An Experimental and Numerical Investigation into Flow Phenomena Leading to Wastewater Centrifugal Pump Blockage

By

Robert Connolly, BEng

This thesis is submitted as the fulfilment for the requirement of the award of degree of

MASTER OF ENGINEERING (MEng)

by research from

DUBLIN CITY UNIVERSTIY

School of Mechanical and Manufacturing Engineering

Supervisor: Dr. Yan Delauré

September 2017

Declaration

I hereby certify that this material, which I now submit for assessment on the programme of study leading to the award of Master of Engineering is entirely my own work, that I have exercised reasonable care to ensure that the work is original, and does not to the best of my knowledge breach any law of copyright, and has not been taken from the work of others save and to the extent that such work has been cited and acknowledged within the text of my work.

Signed: ID No.:

Date:

Dedication

I would like to dedicate this work to my Mother and Father, who have always strived to show me the true value of education, and my wife to be Niamh, for all of your support and inspiration to want to do more.

Acknowledgments

I would like to express my gratitude to Dr Yan Delauré, for all of his help on this project. From the initial concept and development of a research idea to his constant guidance as the research progress, he has always shown great knowledge, patience and persistence that will continue to inspire me for many years to come. Also, thanks to Dr Abdul Albadawi and Mr Mathieu Specklin for all of their technical assistance, without whom, working remotely would have been a very difficult endeavour.

I would very much like to thank Mr Ben Breen, P.D. Manager at Sulzer pumps for providing his great expertise and assistance to this project along with his openness and willingness to foster development within Sulzer P.D. Wexford. Thanks to Mr Stephen Marry, the person who first proposed such an investigation and facilitated learning in a unique and exciting way. Also thanks to Mr Ciarán Quirke for his support in getting this project finished.

Contents

Table of Figures

Symbols and Abbreviations

u	circumferential velocity	$m\,s^{-1}$
r	radius	m
ω	rotational speed	$rad\,s^{-1}$
c	absolute velocity	$m\,s^{-1}$
w	relative velocity	$m\,s^{-1}$
c_u	circumferential component of velocity	$m\,s^{-1}$
E	Euler head	m
g	acceleration due to gravity	$m\,s^{-2}$
H	head	m
ρ	density	$kg\,m^{-3}$
Q	volumetric flow rate	$l\,s^{-1}$
Re	Reynolds number	
u_∞	free stream velocity	$m\,s^{-1}$
L	characteristic length	m
ν	kinematic viscosity	$kg\,s^{-1}m^{1}$
y^+	non dimensional cell wall distance	
U	mean velocity	$m\,s^{-1}$
P	mean pressure	$N\,m^{-2}$
u	instantaneous velocity	$m\,s^{-1}$
p	instantaneous pressure	$N\,m^{-2}$
τ	Reynolds stress	
d	length scale	m
Δ	grid spacing	m
δ	boundary layer thickness	m
B	blockage	
BI	blockage index	
v_{rad}	radial velocity	$m\,s^{-1}$
v_{tan}	tangential velocity	$m\,s^{-1}$
z_{LA}	impeller blade number	
l	length	m
A	area	m^2
$q*$	flow rate relative flow rate at best efficiency point	
z	height	m
β	angle between relative velocity fluid vector and negative impeller circumferential velocity	rad

Abstract

An Experimental and Numerical Investigation into Flow Phenomena Leading to Wastewater Centrifugal Pump Blockage

Robert Connolly MEng.

The work covered in this project had the objective of investigating key factors in single vane pump impeller blockage using both Computational Fluid Dynamics (CFD) and experimental analysis. CFD has been used to highlight flow features leading to such blockage while experiments provided some insight into the significance of certain key parameters, namely radial and tangential velocities within the fluid domain.

This was achieved by testing a large variety of centrifugal wastewater pumps in a purpose built test rig. The test rig was designed and built for this study based on previous research on smaller pumps by Mcevoy et al (1). A suitable test material was used to test blockage performance of the pumps at three different flow rates, Best Efficiency Point (BEP), BEP +30% and BEP-30%. Average blockage performance across the product range was found to vary inversely with duty flow rate, with average Blockage Index (BI) across the tested range varying from 64% at lower flow to 92% at high flow.

A pump which had varying blockage performance with duty flow rate was chosen for further study with CFD. An analysis of the CFD results showed a significant correlation between pump blockage performance and radial velocity components within the fluid domain, specifically in the impeller region. BI within this pump varied from 73% to 100% with increasing flow rate while the local radial velocity (v_{rad}) at the impeller leading edge, where blockage was most prevalent, varied from 1.4 $m\,s^{-1}$ to 6.2 $m\,s^{-1}$. The results of this study highlight large scale flow components and their effect on blockage performance.

1 Introduction

1.1 Pump Reliability and Blockage

In recent decades, there has been a significant improvement in access to clean water and sanitation [Figure 1.1 (2)]. With increasing global populations, the demand has never been higher for reliability in wastewater systems.

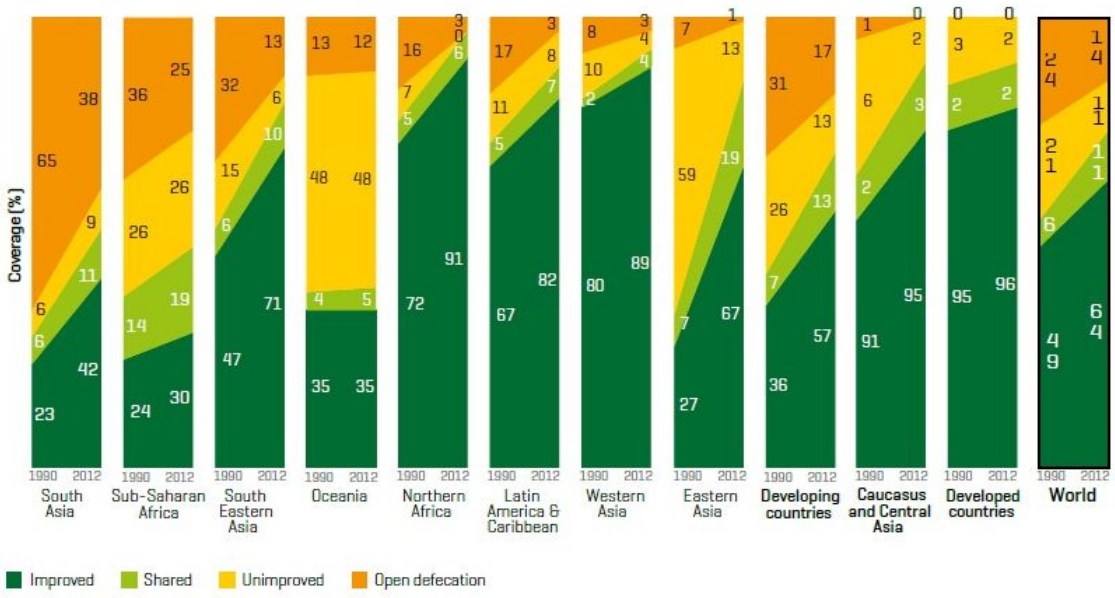

Figure 1-1 Quality of Global Access to Sanitation by Region, 1990-2012. (2)

Wastewater pumps are integral components of wastewater systems, featuring in collection, transportation and treatment processes and as a major contributor to system failures, they are a key concern for reliability (3). Submersible waste water pumps in particular are widely used in collection, transport and treatment of domestic and municipal wastewater and are affected by a number of typical failure modes categorised as thermal, mechanical and hydraulic. The main objective of this research is to better understand the mechanism behind soft blockage, a significant contributing factor to pump failure.

Soft blockage can be defined as a build-up of soft fibrous material inside the pumps hydraulic components. This material will reduce attainable flow rate within the impeller, significantly lowering the hydraulic efficiency of the pump. Many cases have been noted, where soft blockage is so severe within the impeller that the pump becomes bound, locking the rotor and causing a thermal failure. While most pumps are equipped with a thermal overload switch, saving the motor from insulation break down and catastrophic failure, a maintenance crew must attend to the pump to clear the blockage, a costly operation in man hours as well as rental of a substitute pump.

The primary constituents of soft blockage are disposable cleaning wipes and female sanitary products such as panty liners and sanitary towels [Fig. 1-2]. These products increasingly incorporate plastic making them more resistant to maceration when introduced to a pump (4).

Figure 1-2 Samples of Blockage Material, Collected from Pumping Station

Intensive testing was carried out over the course of this research to find a test method that would reflect typical blockage type, mechanism and frequency of that in the field.

1.2 Single Channel Hydraulics as a Blockage Solution

A number of wastewater pump manufacturers have chosen a single vane impeller in order to maintain a large solids passage as required by the Wastewater Committee of the Great Lakes--Upper Mississippi River Board of State and Provincial Public Health and Environmental Managers, or Ten Sates Standard (5). This standard sets out to define a minimum solids passage within a wastewater sewage pump and as it was the first to address the issue of blockage, it is used as a framework for many States in North America.

The single channel ContraBlock+™ impeller (6) is part of a Sulzer pump, optimised to allow free passage of solids through the central channel of the impeller, in addition to complying with requirements for minimum solids passage size as is often specified by many frameworks (7).

The single channel impeller design is also used by many other market leaders such as, Grundfos™, KSB™ and Hydrostal™, some examples of which can be seen in Fig. 1-3.

Figure 1-3 Single Vane Impellers. Clockwise from Top left; Grundfos, KSB, SULZER, Hydrostal.

1.3 Aims & Objectives of the Study

The main objective of this study is to identify the key hydraulic features of a single channel wastewater pump impeller which influence blockage performance. An experimental rig was devised to test a variety of impeller prototypes. The analysis of experimental results is presented in Chapter 4. A CFD study was carried out on one of the impellers tested to analyse flow features in areas critical to anti-clogging performance. The impeller studied was deemed to perform well at avoiding blockage at some flow rates but not so well at others. The aim of the CFD study was to validate the assumptions made as a result of blockage experimentation and gain knowledge on flow physics around the impeller blade. This information will be useful for further research on the topic and in designing next generation hydraulic components.

To achieve these goals the following tasks were accomplished:

1. A standard test sample was established, based on observations from the field in order to reproduce realistic pump blockages and provide a score for individual impellers.
2. A number of off the shelf and prototype hydraulic components were tested in order to provide the largest possible data set for experimental analysis.
3. Visualisation of blockage was carried out using high speed imaging.
4. The ANSYS Meshing and Fluent CFD software were used to compare flow physics around impellers leading to good and bad blockage performance.

Overall this study aims to identify key impeller features for anti-clogging of soft blockages for single vane waste water pumps.

2 Literature Review

2.1 Centrifugal Pumps

2.1.1 Application

The centrifugal pump works by imparting kinetic energy to the fluid with a rotating impeller. The driving torque is generally provided by an electric motor directly connected or coupled to the impeller shaft. Fluid enters the pump through the inlet of the wear ring, and is accelerated by the rotating impeller. This rotodynamic principle causes the fluid to flow outward into the volute which is designed to diffuse the velocity, converting the kinetic energy into flow energy, that is increased pressure, before it is expelled through the outlet or discharge. Pump hydraulic components usually consist of 2-3 primary parts, the impeller, the diffuser and the wear plate (used to prevent leakage of pressure across the impeller blade tip gap) [Figure 2-1].

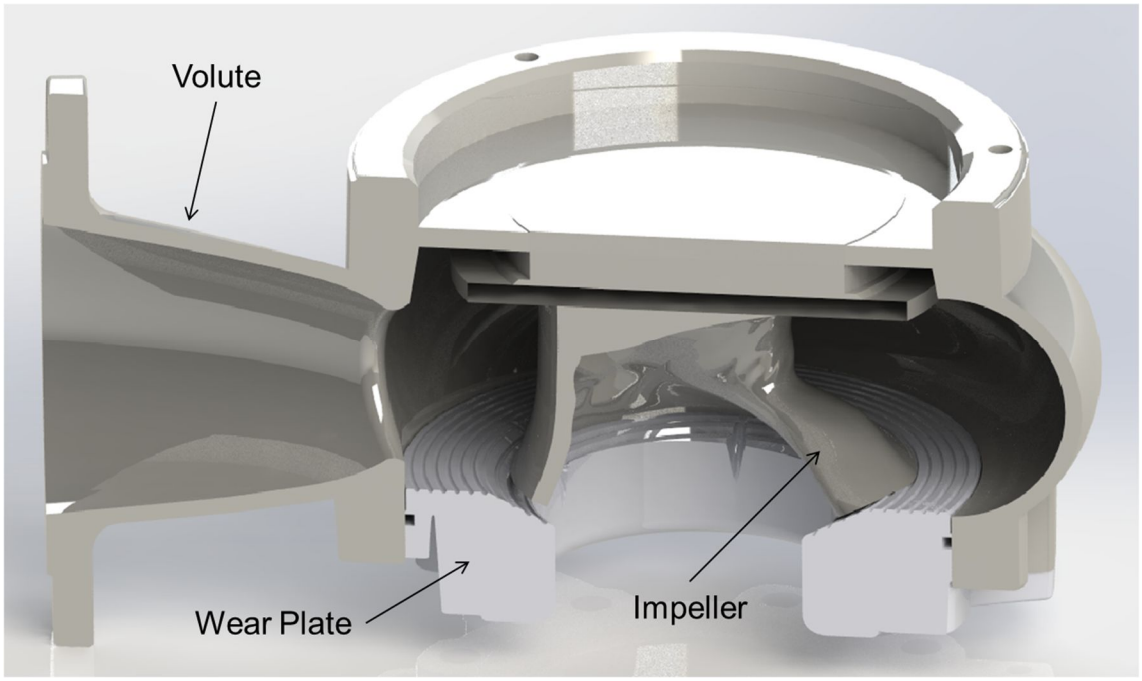

Figure 2-1 Single Vane Pump Hydraulic Components for Wastewater Application with a Volute Acting as the Diffuser

Generally pumps are intended for a specific design point but can be operated within a certain range of flow rates, depending on the machine. Operating away from the pump design point can induce mechanical stresses, pressure pulsations, recirculation and cavitation (8). It is important to be aware of what the limitations are for the specific pump not only based on the operating point but also its intended application. There is great variance in pump application from volatile liquids such as chemical hydrocarbon processing to corrosive and abrasive environments. The pumped medium can also have an effect on the pump suitability, such as multiphase liquid gas mixtures to suspended solids such as waste water and pulp and paper manufacturing. Improper selection can lead to poor pumping performance, excessive wear or pump blockage and rotor seizure.

2.1.2 Principle of operation

Useful theoretical information can be derived from a kinematic analysis of the flow across the impeller. The relevant flow velocity vectors are shown in [Fig 2.2]. These are u, which is the circumferential velocity of the impeller given as $u = 2\pi r\omega$ at radial position r, the absolute velocity c of the fluid at radial position r, w which is the velocity of the fluid relative to the impeller and c_u which is the circumferential component of the fluid velocity (9).

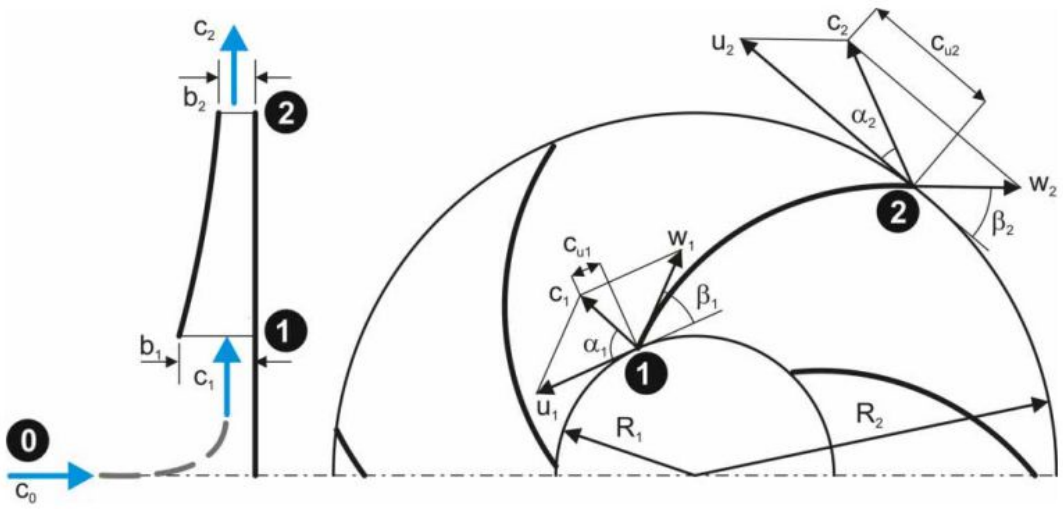

Figure 2-2 Velocity Vector Triangle for a Radial Type Pump (10)

The Euler Head (E) for turbo-machinery is an interpretation of Newton's Second Law in the context of conservation of angular momentum and can be derived from the condition of no pre-swirl (11). E is given by:

$$E = \frac{(c_2^2 - c_1^2)}{2g} + \frac{(u_2^2 - u_1^2)}{2g} + \frac{(w_2^2 - w_1^2)}{2g} \tag{1}$$

In Eq. (1) the first term represents the kinetic energy imparted onto the fluid by the impeller, the second term is the increase in kinetic energy on the fluid due to the circular motion or centrifugal force and the third term is the increase of static head due to the change in relative velocity to the impeller as it passes through the blade passage (12). The torque imparted onto the fluid can be evaluated from the change in tangential momentum flux given as $\rho Q c_{u2} r_2 - \rho Q c_{u2} r_1$. Power can then be expressed as $2\pi\omega(\rho Q c_{u2} r_2 - \rho Q c_{u2} r_1)$. Given that $2\pi r\omega = c_u$, power can be evaluated from $\rho Q(c_{u2} u_2 - c_{u1} u_1)$. Finally, the ideal head, which is the maximum head neglecting pre-swirl and friction losses created by the impeller can be defined by

$$H_{ideal} = \frac{power}{\rho g Q} = \frac{1}{g}(c_{u2} u_2 - c_{u1} u_1) \tag{2}$$

As most pumps must deliver a specific flow rate at a particular head, this formula can provide an initial means for designing a pump. For example, a specific rotational speed and blade angle can be inferred from a required head and delivered flow.

In the classical approach, pre-rotation of the fluid in advance of the impeller can have a significant impact on the calculated head, as the initial velocity and angle of the fluid allows for less energy to be imparted by the impeller (13). This pre-rotation is caused by a pressure drop at the fluid inlet coupled with the fluid finding the path of least resistance when travelling through the pump. It has been shown that the level of pre-rotation varies with the pump operation point (11).

2.2 Boundary Layer in Turbomachine Application

Accurately accounting for the boundary layer in turbomachinery is crucial for understanding and predicting turbulent flow and interpreting the performance of a turbomachine, in particular its loss of efficiency off its design point. It has been shown that turbulent separation within the boundary layer will extend into the free stream flow with increasing stream-wise distance from the transition point (14). Flow separation varies with inlet flow angle, generally occurring on the suction surface. Accurate prediction of this separation is critical to accurate modelling, requiring precise prediction of the formation and growth of the boundary layer (15). The most important aspect being simulating the transition to turbulence within the boundary layer.

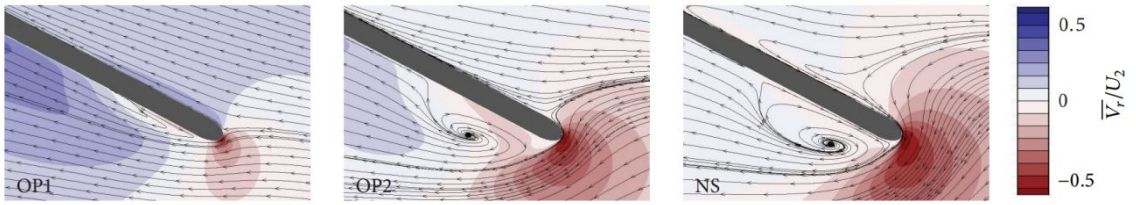

Figure 2-3 Flow separation at the wall of a compressor blade and the extent of the influence of this on the domain, (14)

The boundary layer is a layer where the viscous forces of the fluid cause a large gradient in velocity, extending from the no slip condition where the fluid is the same velocity of the wall, to 99% of free stream velocity obeying potential flow theory (16).

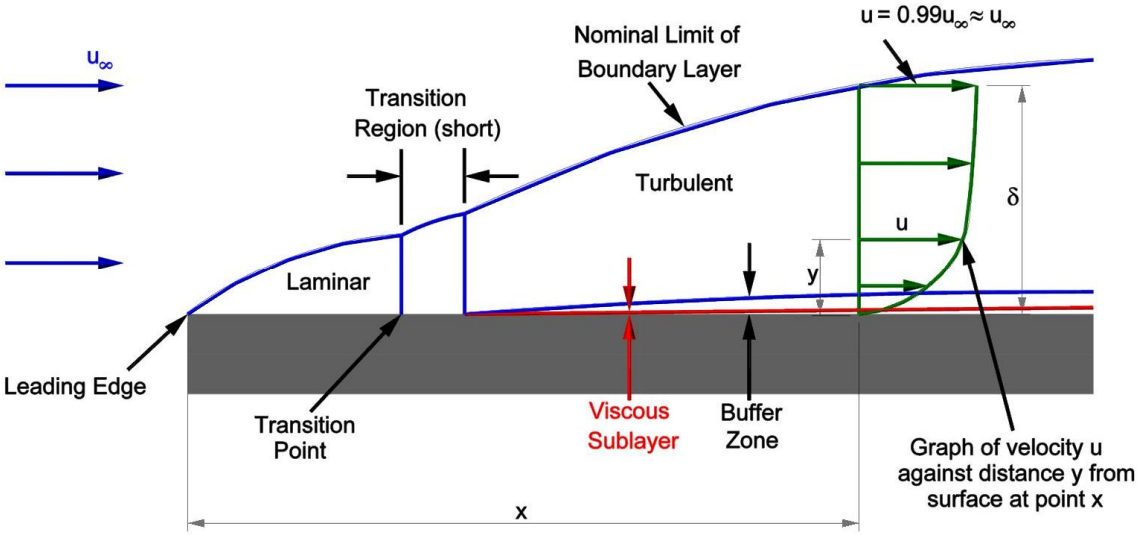

Figure 2-4 Laminar and Turbulent Hydrodynamic Boundary Layers. Note: Scale is greatly exaggerated in Y(streamwise) direction (17)

As the fluid moves along the wall, the boundary layer thickens due to diffusion of momentum under the action of viscous shear. At sufficiently high Reynolds number, the instabilities in the flow evolve and will eventually lead to the transition to turbulence. [Fig 2-4]. Surface roughness and turbulent intensity in the free stream are both significant factors that affect the point at which the boundary layer transitions from laminar to turbulent (12). The most important factor in predicting instability in the boundary layer and eventual transition to turbulence is known as the Reynolds number (Re), which is defined as Eq. 6].

$$Re = \frac{u_\infty L}{\nu} \tag{3}$$

In [Eq. 6] u_∞ is the free-stream velocity, L is the length along the wall and ν is the kinematic viscosity. The Reynolds number can be described as the ratio of inertial forces to viscous forces and thus is a good indicator of the relative strength of viscous diffusion

which serves to stabilise flow instabilities. It is generally accepted that a fluid can be classified as turbulent over a flat plate at $Re \geq 5 \times 10^5$ (17). Predicting the behaviour of the turbulent boundary layer is important not only from the point of view of analysing the boundary layer itself but also, as the turbulent boundary layer has an influence on the entire fluid domain through detachment, the turbulent boundary layer impacts the fluid domain as a whole. Flack et al (18) have shown the high levels of turbulent flow present in the normal operation of centrifugal pumps, ranging 9% inlet turbulent intensity at design point to 19% turbulent intensity at 40% of design flow rate. Additionally, when a pump is operated off the intended design point considerable turbulence and separation is found within the machine (19). As a result, in order to numerically predict the fluid flow in a pump domain it is important to choose a numerical model which accurately predicts the boundary layer and turbulence within the domain. This will be dealt with in the next section.

2.3 Computational Fluid Dynamics for Pumps

Computational Fluid Dynamics or CFD is increasingly used to determine the performance of fluid machines (20). Most modern CFD tools solve the conservative form of the governing equations of fluid flow using the Finite Volume method. Early industrial applications of CFD began in the 1960's when the aerospace industry adapted CFD techniques in order to analyse the performance and improve the design of aircraft and jet engines. Since then, its uses has spread to abroad range of industries including marine engineering (21), rotating equipment (22), automotive design (23), meteorology (24) and biomedical engineering (25). Historically the main hindrance to the application of CFD has been the high computation and associated hardware cost in solving complex flows often present in designs. Since the 1990's there has been a rise in CFD use due to availability of user friendly commercial software packages and increased affordability in required hardware to solve complex fluid problems. (26).

2.3.1 Pre-processing

In order to successfully perform a CFD analysis, it is important to perform some pre-processing work. The first element of this is meshing. A mesh of the fluid volume is

created by dividing the domain into many small volumes. This is usually done from a Computer Aided Design geometry which may or may not be simplified to aid the computation. The mesh enables the CFD solver to solve the discretised partial differential equations necessary to describe the fluid behaviour. The mesh not only governs the resolution of the solution but also influences how stable the solution is as well as what turbulence models can be used (27). Overall the mesh is crucial to providing an accurate domain for the solver to compute the fluid continuum. Some approaches such as near wall treatment allow for approximations of the fluid boundary layer to be made near walls so that the mesh does not have to be refined to very small sizes in order to capture small fluxes in fluid shear near the wall surface (28). One method of meshing is known as the cut cell method. In this method the domain is subdivided into regular orthogonal volumes which can in turn be refined via iterative refinement close to boundaries and can also be morphed to match the wall surface. A benefit of using the cut cell method is that it eliminates the difficulty of using a blocking methodology and is not as tedious as an unstructured tetrahedral mesh (29). The mesh can be body fitted and refined close to boundaries but also as required within the fluid through the use of a number of algorithms such as gradient, curvature and isovalue based refinement (30). When discretising the domain into smaller volumes it is important to have a sufficiently refined mesh near the wall to capture the effect of the boundary layer on the rest of the domain. This can be done by having a mesh so refined that the small changes in shear stress are captured within the computational volume, known as near-wall modelling or by using near wall treatments which estimate the behaviour of the fluid near the wall. A standard way of representing the mesh size close to a wall is to refer to the mesh in terms of y_+, which is non-dimesionalised by the wall distance, friction velocity and kinematic viscosity.

It is also important that the CFD case is correctly set up. On a practical level this involves defining all aspects of the domain that needs to be solved. This practice includes describing walls, inlet and outlet boundaries and interfaces. In setting up the case the user also prescribes controls on the simulation such as how small the timestep should be in a transient simulation or if there is any heat transfer which should be taken into account. The turbulence or other supplementary physical models are also chosen when setting up the CFD case. The user selects a turbulence model based on what they want to observe in

their simulation. Some turbulence models accurately predict high levels of local turbulence while others give more of an approximation over the whole domain (31). The user selects the turbulence or other physical models based on what the desired output of the solver is and what computational cost they are will to accept.

2.3.2 Solver

Solution of a CFD problem fundamentally involves solving the 3 governing equations of fluid dynamics, which are defined by the conservation laws of physics. The most common approach to solving these equations is finite difference formulation with the finite volume method (26). In order to solve the partial differential equations governing fluid flow, the finite volume method involves three steps.

1. Integration of the governing equations for each finite volume in the domain.
2. Discretizing the integrals of the equations into algebraic form.
3. Solution of the discretised equations through iterative means.

When the discretised equations are solved for a general flow variable φ, its component convective, diffusive and rate of creation or destruction in the control volume are resolved (32).

The simulation is calculated by solving the Navier Stokes equations [Eq. 4] for velocity and pressure with the cell centred Finite Volume method. These governing equations can be expressed in the following conservative form;

$$\begin{cases} \nabla \cdot u = 0 \\ \dfrac{\partial u}{\partial t} + \nabla \cdot (u)U = -\dfrac{1}{\rho}\nabla p + \nabla \cdot \left(\tau_{ji} e_i e_j\right) + g \end{cases} \tag{4}$$

Where $\tau_{ji} = 2\nu S_{ji} = \nu\left(u_{i,j} + u_{j,i}\right)$ are the components of the viscous stress tensor with ν the fluid's kinematic viscosity.

For many engineering solutions a turbulence model is required in order to predict turbulent characteristics within the domain. Reynolds Averaged Navier Stokes or RANS

modelling has been extensively used for turbulence modelling in CFD (33). Within RANS models the most common are k-ε, k-ω SST and the S-A model. k-ε turbulence models have in recent years been replaced by k-ω which is much better at predicting near wall shear flow in adverse pressure gradient boundary layers, (34). The Spalart-Allmaras model solves the transport equation for kinematic eddy turbulent viscosity. It is favourable over k-ε as it does not need a geometric length scale which can be difficult to define. Like k-ω SST, the S-A model can improve prediction of boundary layer behaviour under adverse pressure gradients well (35). Originally the S-A model needed $y^+ = 1$, meaning that the mesh had to be at a very fine scale in order to correctly predict boundary layer behaviour. Commercial codes such as ANSYS Fluent have implemented this model with y^+ insensitive wall treatment, meaning that the mesh cell count can now be much lower, reducing computational cost. Implementation of this depends on the y^+, so the wall treatment can be turned on and off depending on the y+ of the mesh. The main weakness of the Spalart-Allmaras model is that like other RANs models it fails to model the formation of small scale turbulent structures (30).

In order to capture large turbulent structures, Scale Resolving Simulation (SRS) models such as Large Eddy Simulation (LES) have become popular in past decades (36). LES resolves large scale turbulence while modelling smaller scales, using the fact that in the inertial range, the isotropic turbulence can be modelled more easily. This makes the LES model quite versatile, as large scale structures can be unique to a certain problem while smaller scale turbulence is more universal. The approach can generate improved resolution of flow in the wake region of a solid object.[Figure 2-4]

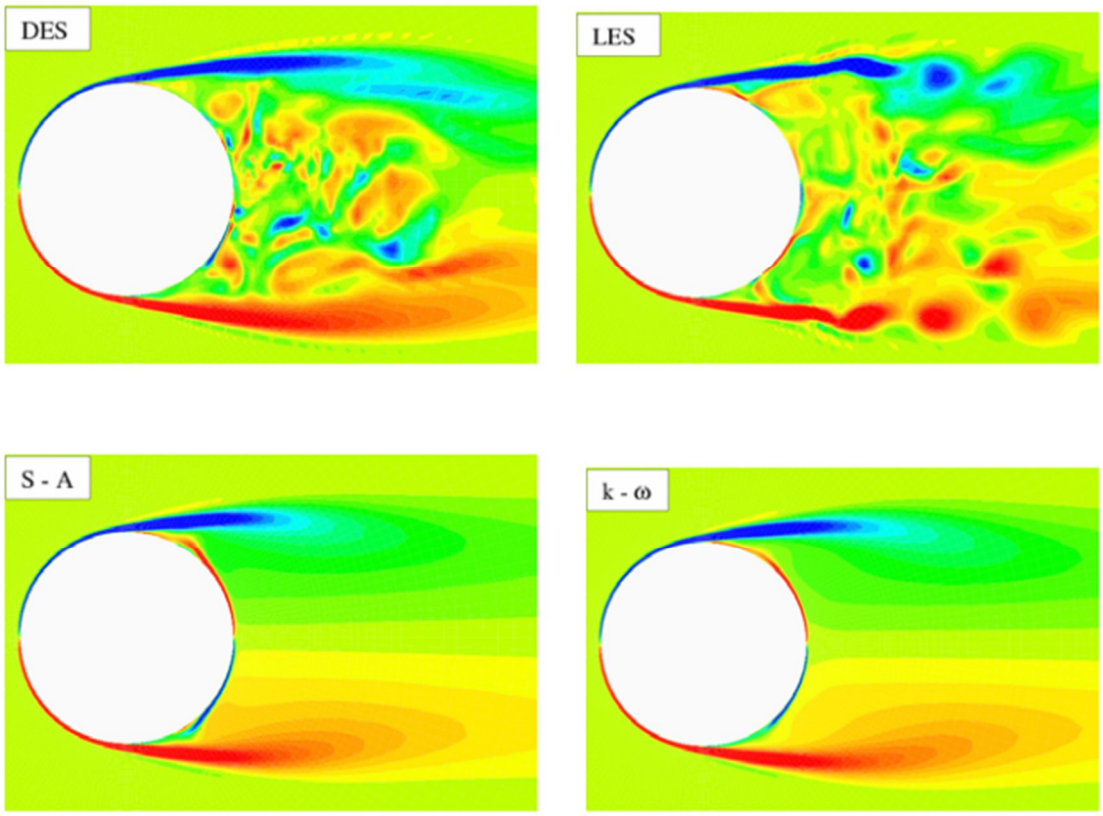

Figure 2-5 Out of plane instantaneous vorticity of flow over a sphere in an azimuthal plane (37)

LES operates by filtering the Navier-Stokes equations by grid volume. In doing this the model resolves the larger scale turbulence while treating the smaller scale with an eddy viscosity model, identically to how RANS models do. Smagorinsky (38) gives the classical LES model as

$$\mu_t = \rho(C_s\Delta)^2 S \qquad (5)$$

Where μ_t is the eddy viscosity, Δ is the numerical mesh local grid scale, calculated as $\Delta = V^{1/3}$ based on the cell volume, S is the strain rate scalar and C_s is a constant. LES models however require a fine mesh to be able to correctly resolve dissipation of turbulence. A coarse mesh will result in molecular viscosity which is too large to correctly predict dissipation and lead to simulation inaccuracy (36).

Use of LES in turbomachinery is rare with the exception of low Reynolds numbers, as in wall bounded flow the mesh near wall boundaries must be refined so that the cell size reduces in proportion to the proximity to the wall, an effect which is compounded with increasing Reynolds number. The key requirement is that the cell size should be within the inertial range of turbulence (39). Detached Eddy Simulation is more common and improves on the negatives of LES through a hybrid approach. This approach switches from RANS to LES and vice versa based on the given grid resolution. This results in the flow at the wall boundary layer being solved with RANS, while the free stream fluid is solved using LES. For free stream flow the DES solution is the same as LES, meaning that in large open flows with little boundary layer calculation, the solution will take the same amount of time as LES. Care needs to be taken of grid refinement in the attached boundary layer, which can cause Grid-Induced Separation (40).

In ANSYS Fluent, DES combined with Spalart-Allmaras replaces the definition of the length scale d in the traditional Spalart-Allmaras formulation with a new length scale $\tilde{d}$[Eq. 9];

$$\tilde{d} = \min(d, C_{des}\Delta_{max}) \tag{6}$$

Where C_{des} is an empirical constant and Δ_{max} is the the maximum grid spacing in the x, y or z directions. It is important to note that in the boundary layer where the mesh aspect ratio is high, parallel to the wall, grid spacing in that direction can exceed the boundary layer height δ. In this case the model works correctly. If however, $\Delta_{max} < \delta$ then the LES model can be activated inside the boundary layer where the mesh size is insufficient to properly capture the turbulence present. Overall, if carefully applied it is clear that SA-DES or similar SRS are efficient and robust methods to solve complex free stream turbulence and wall boundary layer in CFD.

2.3.3 Turbulence Modelling

Turbulent flow is by far the more prevalent regime in everyday industrial simulation studies due to the fact that universal laminar flow on a macro scale is quite rare. [Fig. 5-1] shows the amount of publications and citations which refer to the terms “turbulent fluid” compared to “laminar fluid” since 1950.

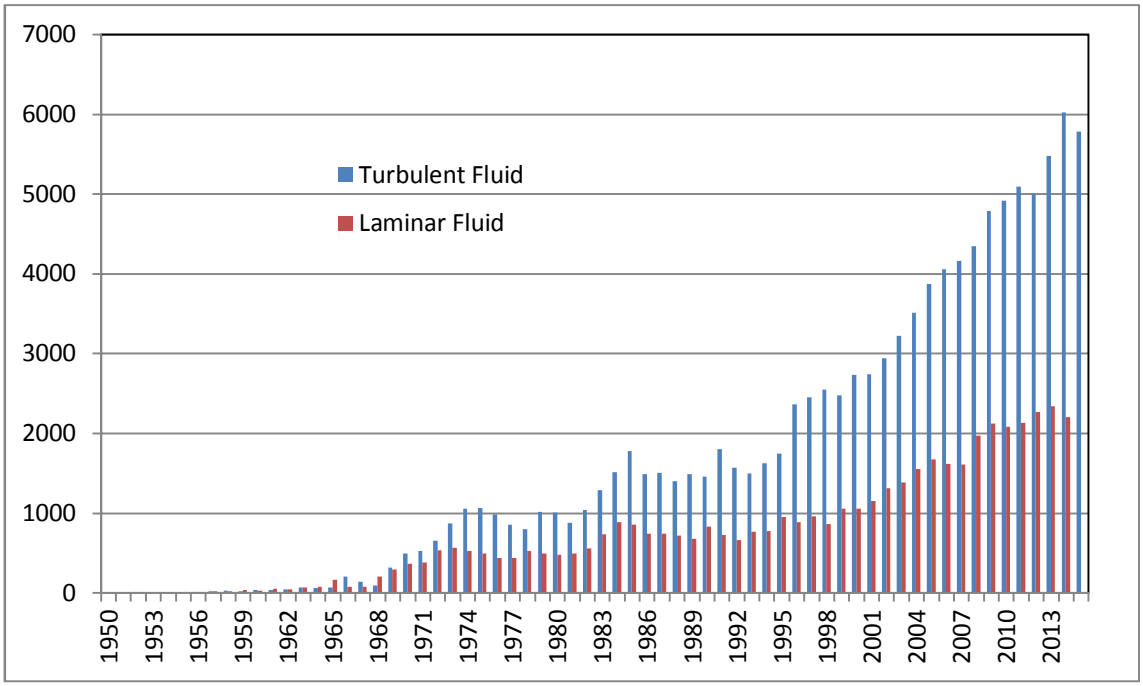

Figure 2-6 Published items and citations 1950-2015, (41)

In order to study the influence of the fluid on rag behaviour it was deemed necessary to include a turbulence model in the CFD simulation. A Spalart-Allmaras Detached Eddy Simulation turbulence model was used in this study in order to correctly solve the fluid in the boundary layer by approximation, as well as capturing the larger scale free turbulent boundary behaviour and shed vortices which can occur in turbo-machinery (42).

2.3.4 Rotor-Stator Interaction

Until recently standard applications of CFD to turbomachinery would have typically used quasi-stationary or frozen rotor methods. The frozen rotor technique has been valuable to industry as it gave a way to determine the performance of rotating equipment in an efficient way. It relies on a Multiple Reference Frame (MRF) formulation in which rotation is treated in a region wise routine. The stator and rotor are simulated in a steady-state approach whit the rotor solved in a rotating reference frame so that Coriolis and centrifugal forces must be accounted for. The main issue with the frozen rotor method is that by definition vortex shedding from the impeller trailing edge cannot be transferred correctly from the rotating impeller to the stationary volute domain (43). One way of accounting for this is to carry out a frozen rotor simulation with the rotor in multiple positions. While the Frozen rotor approach can capture some turbulent transfer, it is found to be less accurate at predicting shear layer interaction between stator and rotor, such as in a centrifugal pump. The lack of periodicity implicit in single vane hydraulic components also makes this approach impractical. As a result, it was determined that a frozen rotor approach would not be suitable to capture all of the relevant flow features in order to view possible blockage mechanisms within the fluid.

Due to advancements in computing power, it is becoming increasingly viable to perform full transient simulations on turbomachinery which accounts fully for the rotating impeller. For the CFD case in this study a General Grid Interface (GGI) is used for the transient formulation. Jasak et al (44) describes the GGI as a method for implicitly coupling the rotating and stationary domain interface without the need for perfect cyclicity in both mesh structures [Fig 2-4]. The discretisation of the governing equations requires that the fluxes between cells across the GGI be calculated at every time step. When the faces of adjoining cells at the interface overlap exactly, the calculation is unaffected by the rotating zone. However, it is more common that as the zones rotate relative to each other, the cell face from one zone will not exactly match with the faces from the neighbouring cell across the interface. The portion of the flux directed into each neighbouring cell must then be calculated. This is done on the basis of face area fractions.

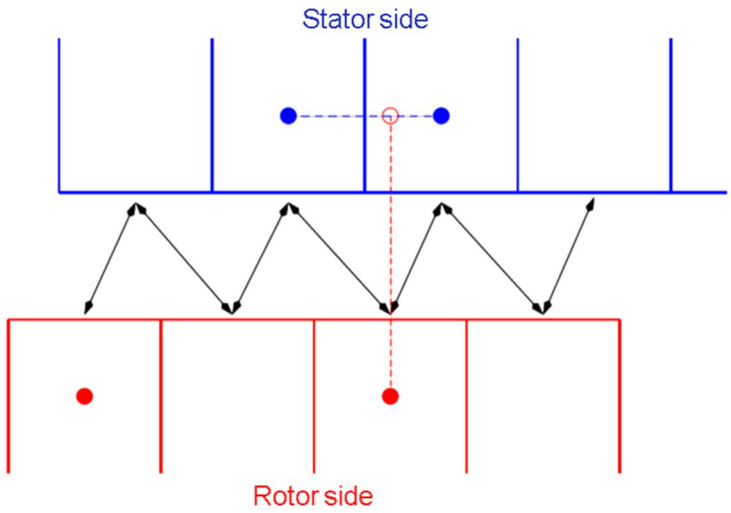

Figure 2-7 GGI communication between rotor and stator (44)

A review of the above literature was essential to understanding the intricacies of both the physical operation of centrifugal pumps and the numerical methods used to study fluid flow both in general and specific to turbomachinery. Both physical and numerical fields are combined in this study to gain insight into the results of experimental research, propose theories and ultimately test these theories with Computational Fluid Dynamics.

3 Blockage Testing

3.1 Test Method

An acceptable and realistic test method was needed in order to test a wide range of pumps with material that accurately reflects the conditions experienced by pumps in the field.

The test method used in this study was based on that of McEvoy, (1). Tests are repeated over three different flow rates covering typical operating range of wastewater pumps. The volumetric flow rate at the Best Efficiency Point, Q_{bep} is used, as well as at flow rates 30% above and below this value, $Q_{bep+30\%}$ and $Q_{bep-30\%}$ respectively. Three independent tests were repeated at each flow rate with each test run involving the introduction of 10 blockage samples, as described in Section 3.2. A score is assigned for each flow rate, based on the percentage of samples passed by the pump. The average of these three flow rates gives the pump blockage index (BI). The BI is defined as the ratio of samples passed, B_P to the total number of samples introduced, B_i, $BI = \frac{B_p}{B_i} \times 100$.

Pumps tested are of standard type used in municipal wastewater application as would be seen in the field.

In order to supplement and further inform the research, a high speed camera is used to record the hydraulic passing the rag and blocking. The camera, which is capable of recording at 1000fps, provides some insight into how the test material interacts with both the fluid and the pump impeller surface in addition to the forces which act upon it.

3.2 Blockage Material Samples

An analysis of blockages was carried out on three sites and samples taken for classification.

Most blockages contained cloth of non-woven synthetic fibres, typically the outer casing of sanitary towels and disposable domestic wipes. Initially a heavy duty sanitary towel was used as a test material. However this was found to degrade rapidly in the water,

affecting visibility and prohibiting high speed filming of tests. A filtration system was introduced into the test tank but emptying the filter is time and labour intensive. The filter, when blocked, can also increase system head, changing the duty test point. Changing the water in the tank was not seen to be sustainable as the volume was too great, taking approximately one day to drain and refill while also being wasteful of water.

A study was carried out to determine a good substitute for the original test material based on a number of factors, with extra consideration being given to blockage behaviour and suspended solids. These factors are as follows;

- Size
- Blockage Behaviour
- Bulk of Storage
- Availability
- Suspended fibres in medium post test

Of the 17 different sample types a short list was made of 3 potential replacements for the test material. This shortlist was determined through testing, carried out using the most successful pumps to pass solids in the medium size range, 9kW to 3kW.

The shortlisted items were then tested against a number of different pumps of both large and small size in order to determine the similarity of blockage type with the original test material. Macrotek was chosen based on these criteria, see Table 3-1. A validation study was then carried out to ensure comparability of Macrotek vs. Kotex across a range of pump sizes, Table 3-2.

Table 3-1 Shortlist of test materia

Test Material	Size	Blockage Behaviour	Storage	Availability	Fibres	BI	Rank
Kotex	265X90	10	5	7	1	93	4
Wypall X70	410X320	8	7	9	8	47	2
Macrotek	228X228	9	9	9	9	63	1
Face Cloth	310X310	7	5	6	6	80	3

Table 3-2 Validation of replacement material across pump size range

Test Material	Pump	Size	-30%	Qopt	30%	BI	Vs. Kotex
Kotex	1	265X90	93	93	100	96	100%
Macrotek 9X9	1	222X222	83.3	90	93.3	89	93%
Kotex	2	265X90	57	100	100	86	100%
Macrotek 9X9	2	222X222	57	90	90	79	92%
Kotex	3	265X90	70	96	100	88.7	100%
Macrotek 9X9	3	222X222	38	58	98	64.7	73%
Kotex	4	265X90	23	23	40	29	100%
Macrotek 9X9	4	222X222	7	7	20	11	38%
Kotex	5	265X90	63	97	100	86.7	100%
Macrotek 9X9	5	222X222	30	47	93	56.7	65%
Kotex	6	265X90	70	73	80	74	100%
Macrotek 9X9	6	222X222	14	20	32	22	30%

3.3 Test Rig

A test rig was built for the purpose of this study in order improving on a previous version. The new test rig, shown in Figs 3-1, 3-2, increases the range of pumps that can be tested and scored for blockage index. In order to test larger pumps the test rig contains a DN300 test line in addition to a DN150 line for smaller pumps. The volume of the tank is $5m^3$ with a cross sectional area for return flow of $4.2m^2$. This tank is designed specifically for performing blockage test on pumps but also with the option to be expanded to conduct performance testing if required. The design of the rig was based on a smaller model from McEvoy et al with modifications made for the extra mass of the increased tank volume, acceptable recirculation rates at high flow and sufficient return flow to avoid overflow. The tank was manufactured off site by a local fabricator and assembled on site on sections. The modular design of the tank left flexibility for additional sections to be added in the future for the purpose of increasing the fluid volume.

The test hardware on the tank includes flow-meters and pressure transducers on both lines in order to accurately establish the duty point at which the pump is being tested. A pinch valve is located between the pressure tapping and flow-meter to maintain the desired flow rate. Perspex windows are located directly below the coupling point of the test pump and at the tank sides. This permits visual inspection and recording of rag behaviour as it interacts with the pump suction stream and impeller.

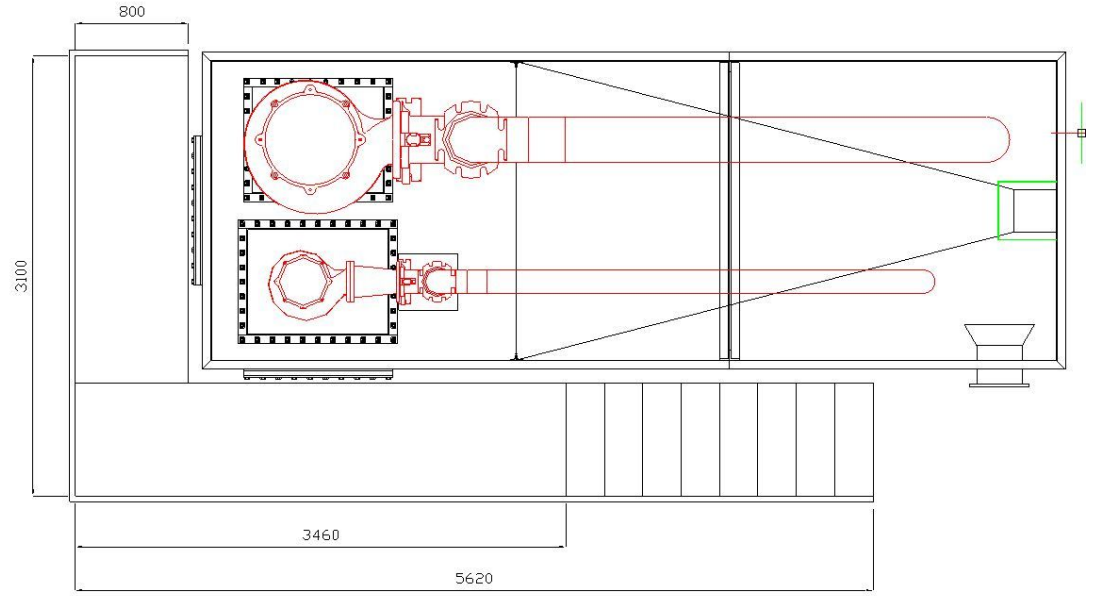

Figure 3-1 Plan View of Blockage Test Tank Including Pipework and Test Pumps

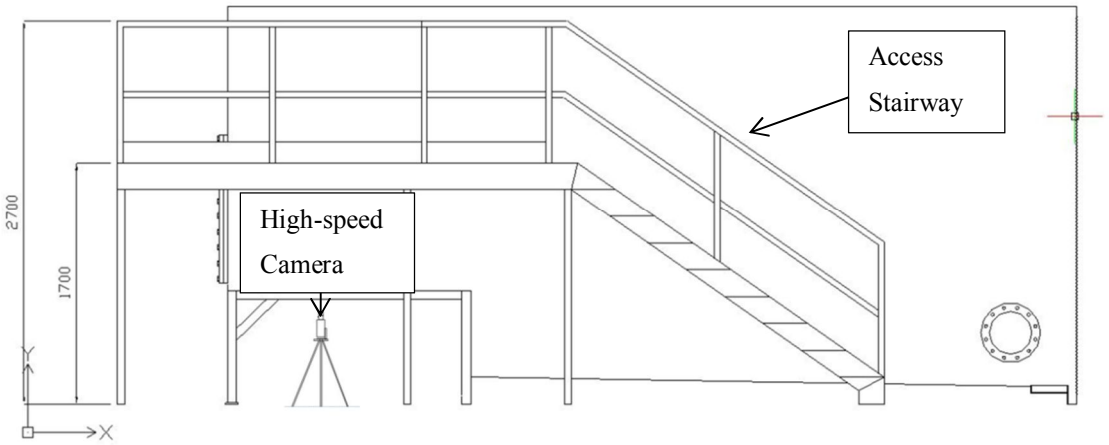

Figure 3-2 Elevation View of Blockage Test Tank with High Speed Camera Beneath Viewing Section

The high speed camera in the blockage test rig was used to compare blockage behaviour of each of the shortlisted sample materials at high flow, low flow and best efficiency point.

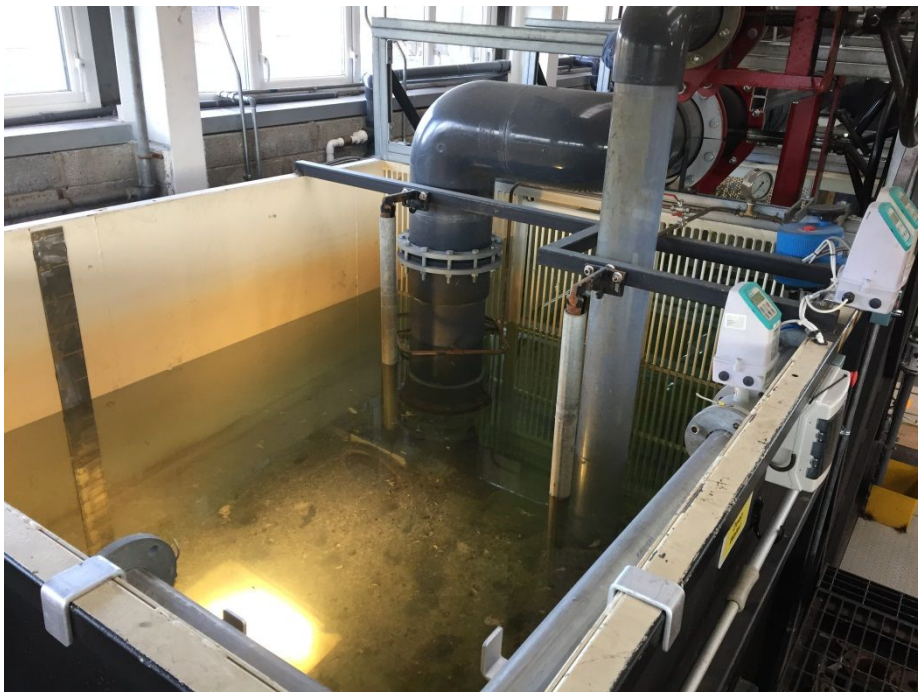

Figure 3-3 Pump Section of Blockage Test Tank Showing Illuminated Viewing Section and Discharge Pipework

3.4 Blockage Classification

A number of types of blockage were observed by McEvoy in a previous study (1). It was decided to treat these blockage types in two separate categories, hydraulic and mechanical. This study will only deal with those which can be classified as hydraulic. Observations were made, using the high speed camera to identify blockage type. Three blockage types were classified in the hydraulic blockage category. These blockage types are volute recirculation, impeller eye and leading edge blockage. By far the most frequent type of blockage to occur is at the impeller leading edge.

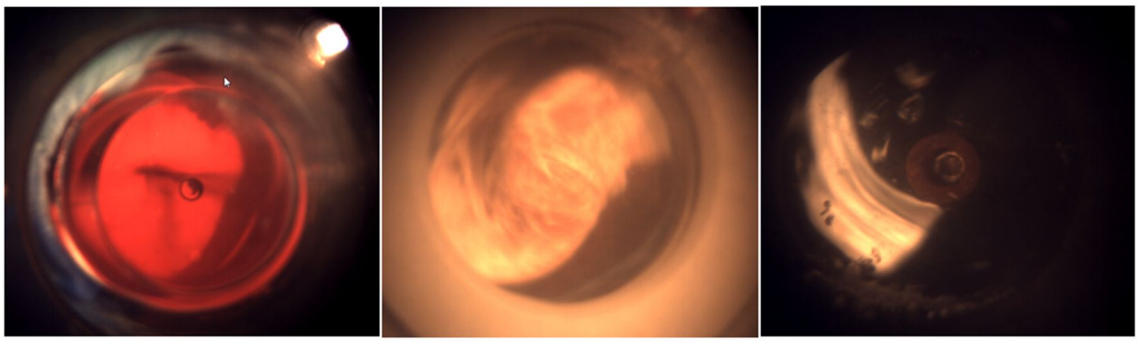

Figure 3-4 Hydraulic Blockage Types. (Left to Right) Volute Recirculation, Impeller Eye and Leading Edge

Another type of blockage identified is known as tip gap blockage, where the rag jams between the impeller and bottom plate. This was not included in this study as it is primarily caused by mechanical forces and occurs in a region which is very difficult to study in CFD. The gap in this area is typically 0.3mm with one face stationary and the other rotating. As a result there are very high levels of fluid shear present in a very small domain which would require an impractically fine mesh to conduct a meaningful study.

4 Experimental Results and Discussions

4.1 Experimental Results

A large number of pumps over a significant range of application sizes were tested as part of the experimental analysis of pump blockage. In all, 36 pumps were tested, each at 3 different flow rates. The results were then analysed for correlations relating to a number of different factors.

4.2 Observations from High Speed Camera Testing

McEvoy (1), states that leading edge blockage is the most prominent type of blockage found in this type of centrifugal pump in wastewater application. It was decided to focus this research on the contributing factors to leading edge blockage. A large number of observations were made of pump blockage with the high speed camera equipment at the specified test flow rates. When passing through the pump, the rag was observed to come through the inlet, along the impeller suction surface, past the impeller trailing edge, around the leading edge and out of the volute via the discharge after one or two rotations [Figure 4-1]. A typical process of leading edge blockage was the rag being caught either side of the impeller leading edge as a result of not being moved outwards quickly enough. The action of consistent leading edge blockage was observed and recreated in 3D CAD. Figure 4-2 shows how the rag is seen to enter the pump towards the suction surface via the inlet, in the relevant reference fame. With the flow split between the suction and pressure surfaces, it was noted that rag orientation on entering the pump can have an impact on blockage, as per Fig 4-2. [i]. If the rag is found to be simultaneously distributed across the streamlines towards both the pressure and suction surfaces then it is likely to block, [ii]. As the rag approaches the impeller surface, it is already being streamed along both pressure and suction surface by the fluid flow, which is relatively slower than the impeller rotational speed, [iii]. The rag will then become stuck strongly to the impeller surface by its own inertia, with forces in equilibrium between pressure and suction side, [iv].

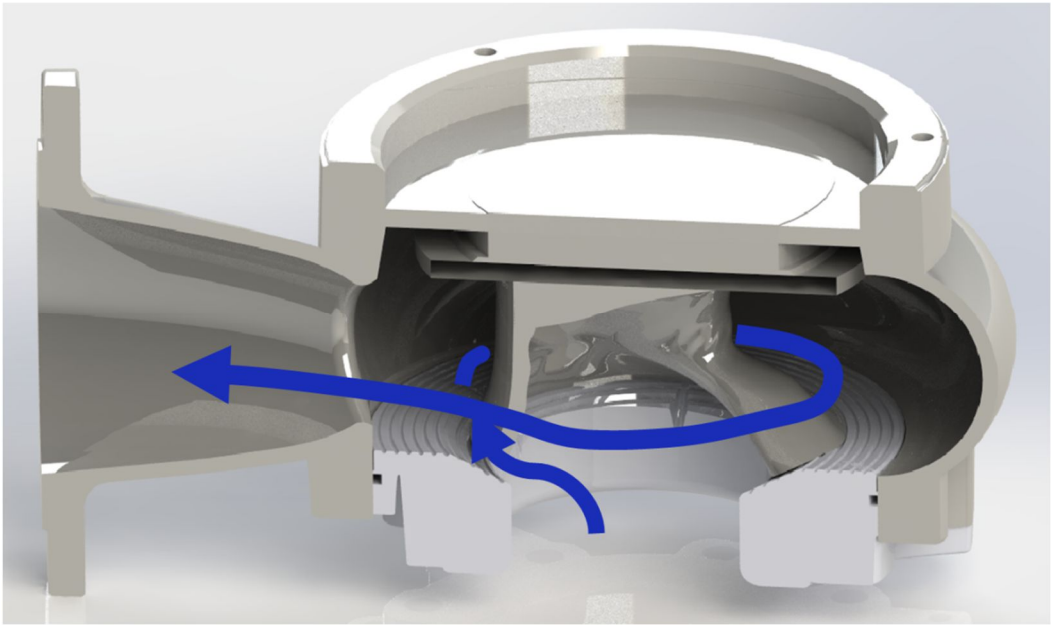

Figure 4-1 Typical flow path through pump in the stationary frame

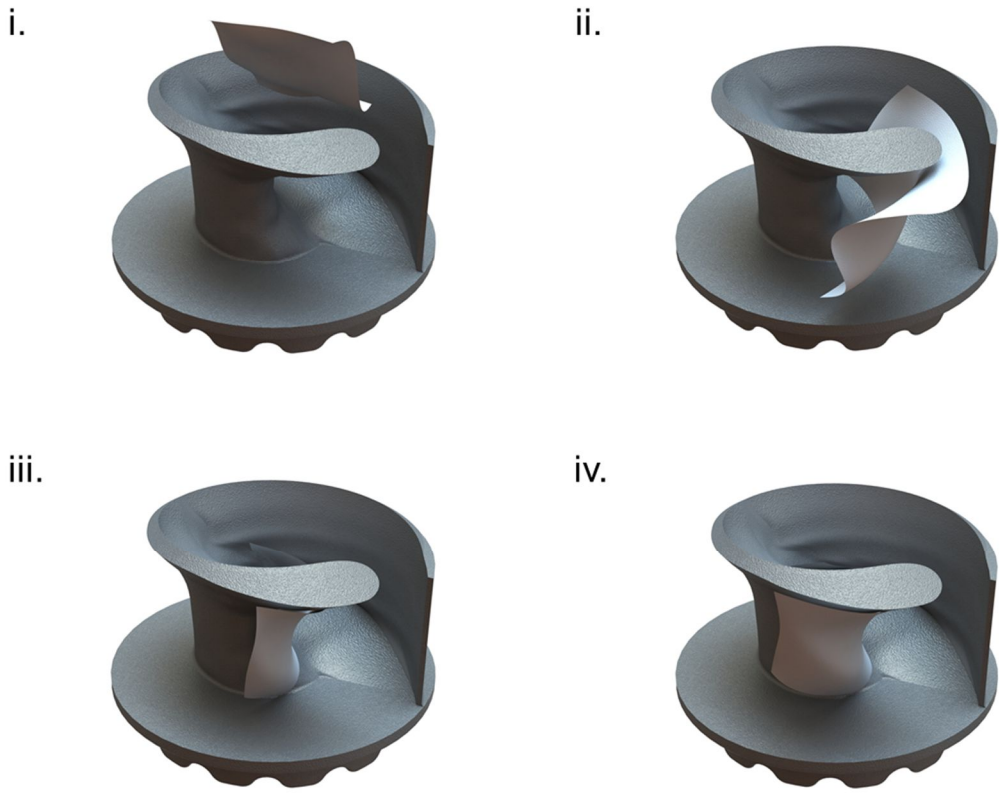

Figure 4-2 Stages of rag blockage based on experimental observation

4.3 Discussion of Experimental Results

The current range of pumps available, which vary from 1.5kW to 30kW in motor shaft power, were tested at each of the three flow rates, Q_{bep} $Q_{bep-30\%}$ and $Q_{bep+30\%}$. An average of these results was then taken and a direct correlation between relative flow rate and Blockage Index(defined in Section 3.1) was observed.

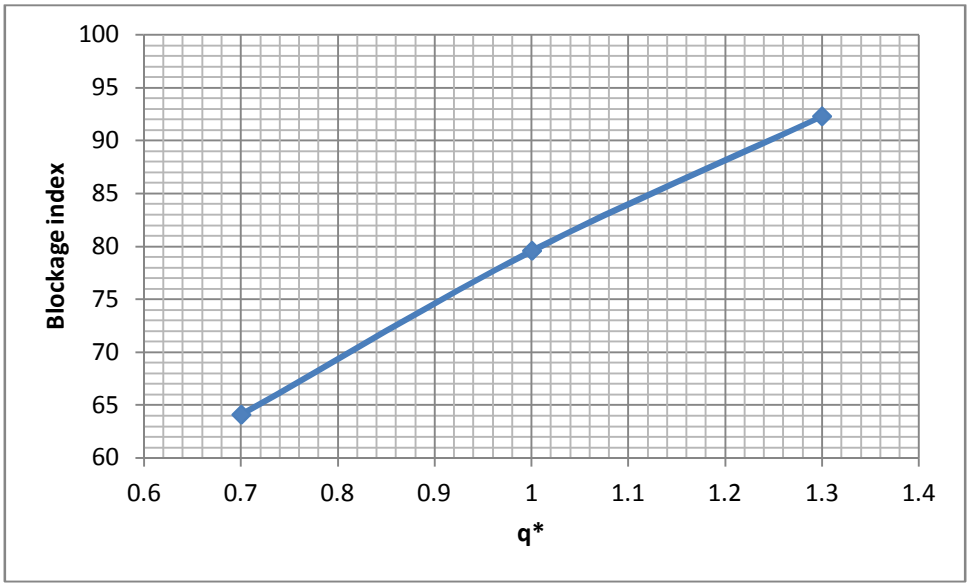

Figure 4-3 Averaged blockage performance at multiple flow rates

The anti-clogging performance should increase in proportion to:

- The volumetric flow rate Q or the average radial flow velocity over the impeller opening between its leading and trailing edge v_{rad}: High flow rate through the pump will strongly influence the speed of ejection of the rag out of the impeller region into the pump volute.

- The tangential flow velocity of the impeller opening v_{tan}: If the flow transporting the rag as it is ejected into the volute past the trailing edge is at a higher tangential velocity than the speed of the leading edge, it is less likely to be caught up by the impeller before it is fully transported into the rotating flow of the volute region. This however is difficult to quantify from purely geometric consideration.

The opposite effect should occur by increasing

- The area of the gap A between the impeller leading and trailing edge: the smaller this area the stronger the flow ejection velocity which helps to clear the rag off the impeller. The number of blades z_{LA} may also have an effect as an increase in z_{LA} is likely to lead to a smaller gap. z_{LA} however, also impacts on the general hydrodynamic performance, but the effect in this case is difficult to qualify.

- The length of the rag, l: as the rag flows out of the interior part of the impeller, past the trailing edge into the volute it finds itself in a flow which may be circulating around the volute at lower speed than the leading edge of the impeller. If this is the case the impeller can catch up with the rag, eventually leading to a rag wrapping itself around the impeller. This is more likely to occur for a longer rag in particular if its trailing end is kept back by interaction with the inlet wall or the wear plate. It may be pinned against the wall by pressure or exposed to shear stresses due to friction against the wall surface.

- The rotational speed of the impeller ω: the faster the impeller for a fixed inlet flow rate, the more likely it is to catch the rag. An increase in the rotational speed of the impeller can also alter the hydrodynamic performance affecting the ratio of radial to tangential velocity at the exit from the impeller which is key to the anti-clogging performance. This however is difficult to quantify without taking into account the volute and impeller geometries and details of their effects on the flow. This would suggest that a purely statistical analysis focussing on the rotational speed may fail to show strong correlation.

To summarize it can be expected that the likelihood of clogging should increase in proportion to A, l and possibly ω and inversely to Q. A non-dimensional rag incidence can be defined:

$$RI = \frac{Al\omega}{Q} = \frac{dhl\omega}{Q} \tag{7}$$

An average of the experimental results of three different pump families at three different flow rates shows an inverse correlation between rag incidence and blockage index [Figure 4-4].

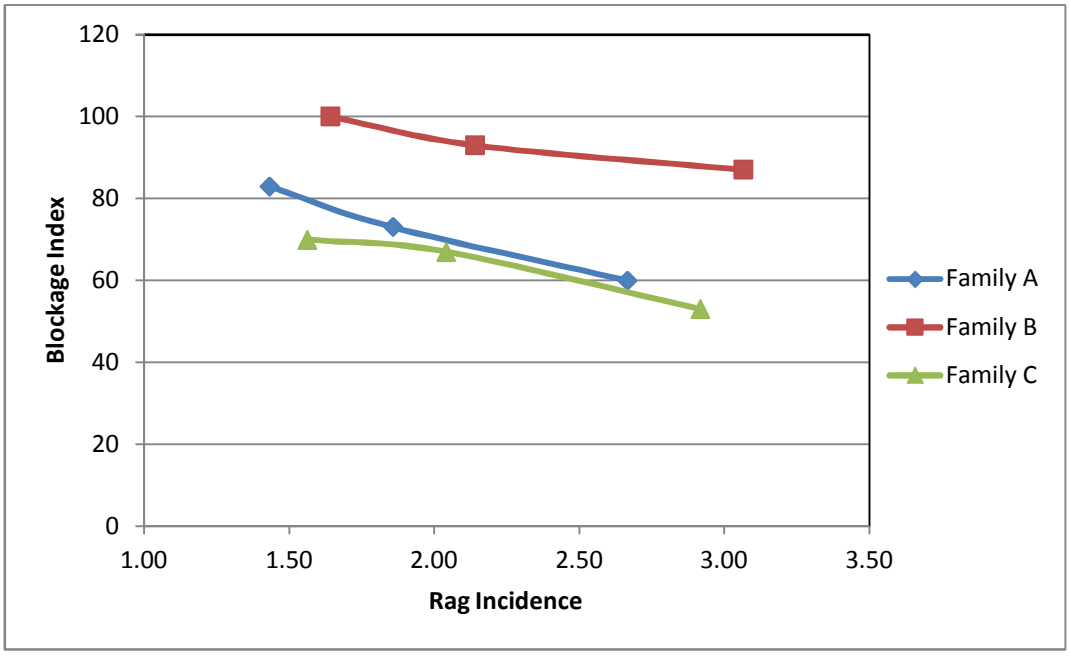

Figure 4-4 Rag Incidence vs. Blockage Index for 3 different pump families

Although ensemble averages suggest a non-negligible dependence of the Blockage Index on Rag Incidence, it must also be recognised that there is significant scatter in the data. This may be as a result of noise in the experimental method, Figure 4-5. Blockage Index

does not account for more complex interactions of rag and wear plate or variance in rag orientation at pump entry.

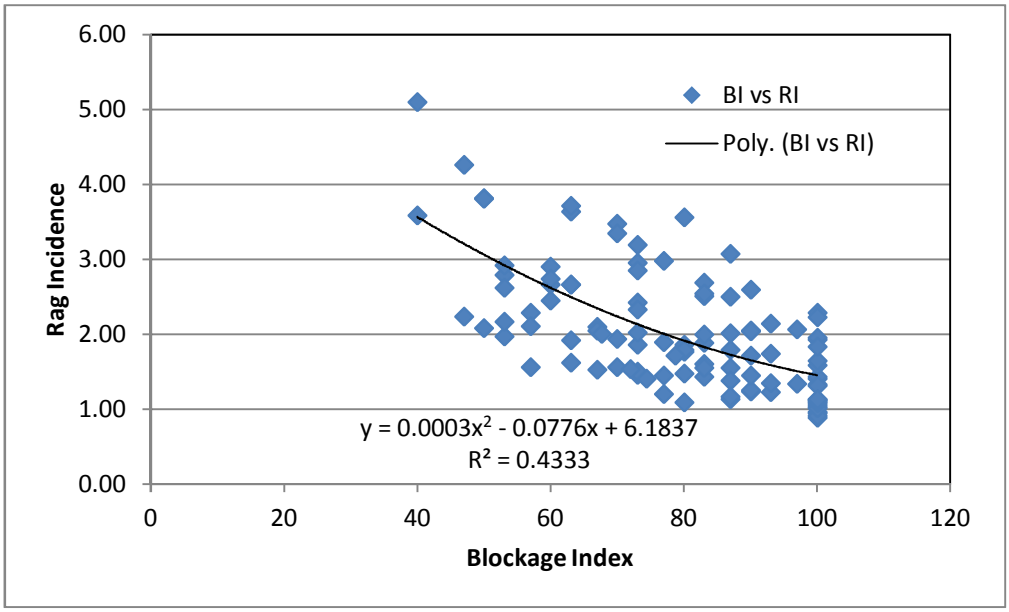

Figure 4-5 Blockage Index vs. Rag Incidence for full data set at each test flow rate

It can be hypothesised from the above results that as the rag moves through the pump driven by the through flow of the fluid, it is reasonable to assume that it is intercepted by the impeller leading edge before it can be carried to a radial position outside of the leading edge. Once it has become trapped on the leading edge the rag will not be moved easily. Forces driven by both the fluid inertia and impeller rotation will ensure adhesion to the impeller.

5 CFD Simulation

5.1 Pump Selection

Based upon the results in Chapter 4, it was decided to carry out a study using Computational Fluid Dynamics. This provided an insight into how the flow behaves within the pump and how it influences blockage. The intention was to find elements of the flow which would explain why blockage is more probable at low flow rates than high flow rates, that makes physical sense for how a rag would behave in the pump. A pump which had been tested experimentally for blockage resistance and performance was selected for the study. This pump resisted blockage at $Q_{BEP+30\%}$ with BI=98%, while still having some blockage at $Q_{BEP-30\%}$, BI=38%. High speed camera footage also provided insight into blockage type with regards to flow conditions at the pump impeller. Comparing calculated Head with the QH performance curve also validated the simulation against experimental performance data.

It was decided to simulate the pump at a number of flow rates in order to have a good comparison with the experimental results. The points chosen were Q_{BEP}, $Q_{BEP+30\%}$ and $Q_{BEP-30\%}$.

5.2 Numerical Method

Computational Fluid Dynamics is used frequently in industry to determine the performance of hydraulic components. It can be more cost effective to carry out a CFD study on designs when compared with prototyping and physical testing (20). Furthermore post processing in CFD allows for easy flow visualisation, a task which traditionally would have been carried out using dyes or particles injected into the fluid, or optical methods such as Particle Image Velocimetry, which can show limited data (45).

Pumps and other rotating equipment present several specific challenges when numerically modelling using CFD. The specific pumps dealt with in this study create a challenge as the flow field in the pump domain is highly time dependent on a number of ways. Kaupert (46) reported in 1999 on the highly transient pressure field within a 7 blade centrifugal pump, while DeSouza (47) demonstrated computational results which had pump periodic pressure fluctuation by as much as 30%.

5.3 Solution Scheme

The Navier Stokes equations are solved using a segregated approach whereby the momentum and continuity equation are solved sequentially in iterative processes. Since the pressure term is not present in the continuity equation various pressure velocity coupling methods have been developed. The Pressure Implicit with Splitting of Operators or PISO pressure velocity coupling scheme as described by Issa (48) was used in the solution. This scheme is considered to be robust and accurate for a case such as this, where convergence can be difficult (49). In cases with small time steps such as this, the PISO scheme can be more computationally costly than other schemes but this was deemed to be worthwhile due to the schemes accuracy and robustness. The PISO algorithm operates by adding a predictor step and two additional corrector steps to the SIMPLE algorithm. Although additional steps are involving in solving this approach, it has been found to be not as computationally costly as would be expected (26).

5.4 Mesh

A hexahedral mesh was provided for the study (50) which contained ~65 × 10^5 cells with a wall adjacent mesh characterised by y^+_{mean} of 116, y^+_{min} of 6 and y^+_{max} of 300on the impeller. In this study a mesh convergence and time convergence study was carried out in order to have confidence in the results while ensure the most efficient numerical solution. A review of literature has found that a similar y^+ resulted in accurate prediction of pressure coefficient predictions with an identical turbulence model (51). The mesh contains 4mm cells in open areas with proximity refinement at the impeller in four steps where cells are split 8 times. 4 prism layers with a growth rate of 1.2 are used in the inflation layer. A comparison of this mesh and a refined version found a small difference

between the two in predicting pump head [Fig 5-2] For a qualitative study such as this one a small difference in predicted head is acceptable as it is only desirable to examine flow features and not predict the pump curve.

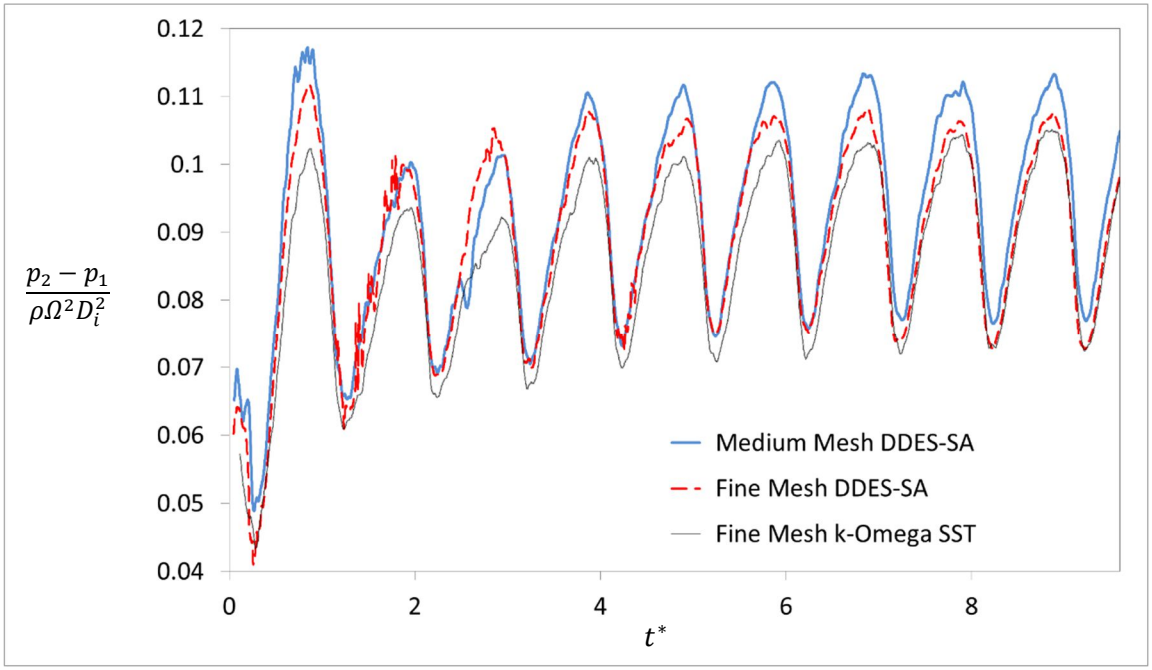

Figure 5-1 Periodic oscillations of non-dimensional pump head against normalised time $t^* = t/T$ where T is the period of impeller rotation (50)

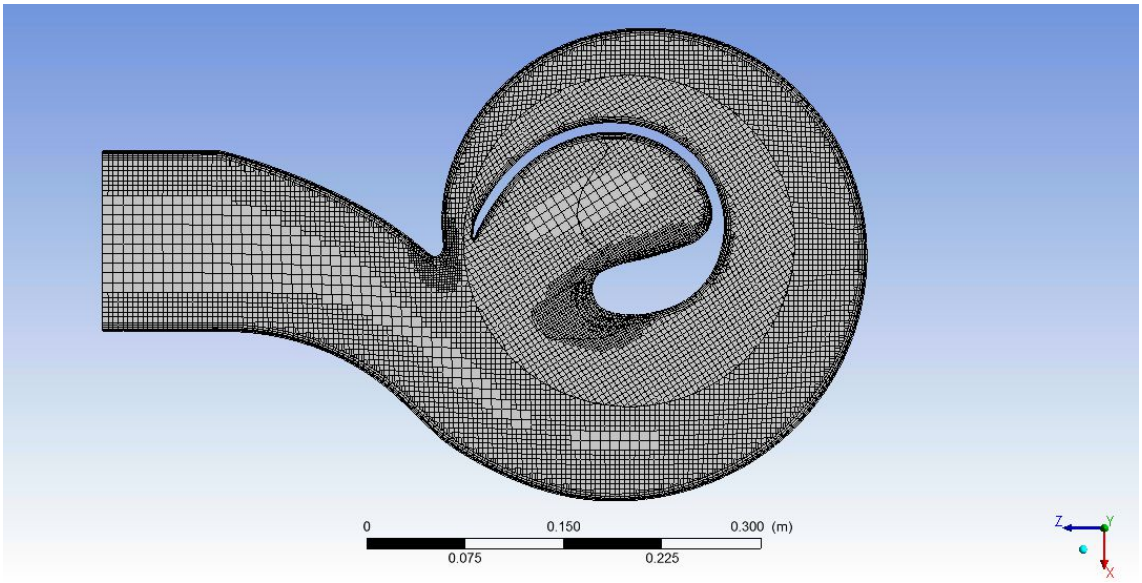

Figure 5-2 Planar sample of the mesh including adaptive refinement and inflation layer on impeller and volute walls

5.5 Pump Geometry

The pump used in this study had an extended inlet domain [Figure 5.4]. This was done in order to relax the need for very well defined turbulent boundary conditions at the pump inlet. As there is a sump the computation has the entire inlet domain to resolve turbulent boundary conditions prior to the flow reaching the inlet pressure plane. The pump head is calculated between the inlet pressure plane and the outlet boundary. The distance from the pump inlet to the bottom of the sump is given as H/D = 1.17. Albadawi (52) conducted an experimental study with varying ratios of H/D at the Sulzer test bed and the ratio used was found to have no impact on pump head as can be seen in [Fig 5-4, Fig 5-5].

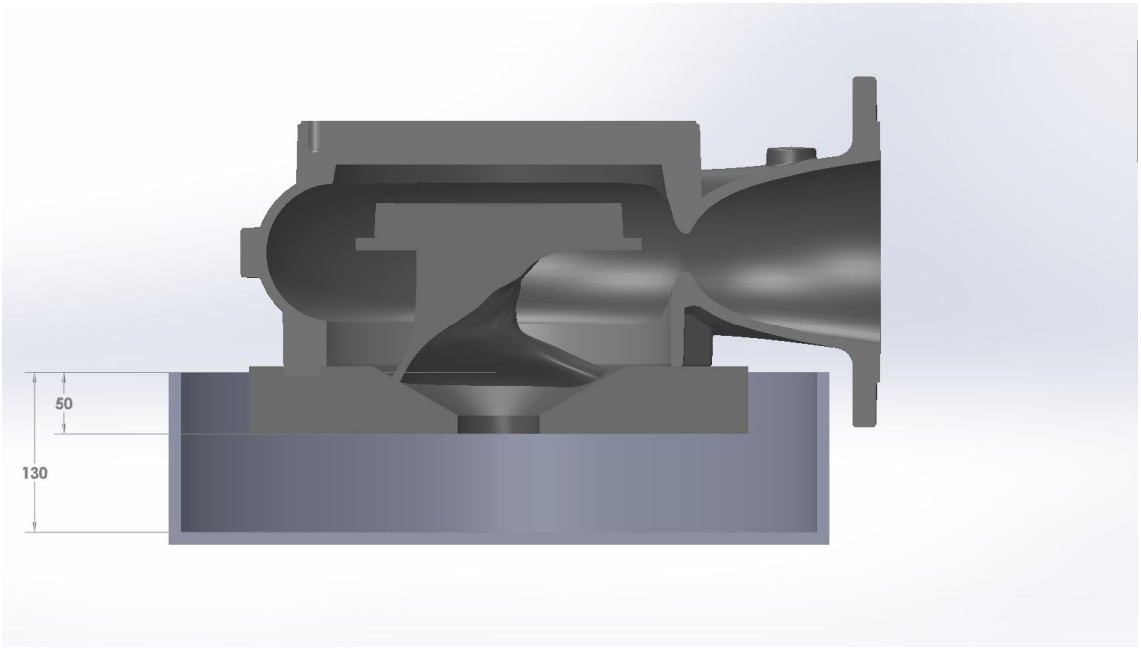

Figure 5-3 Varied H/D Ratio for Inlet Domain.

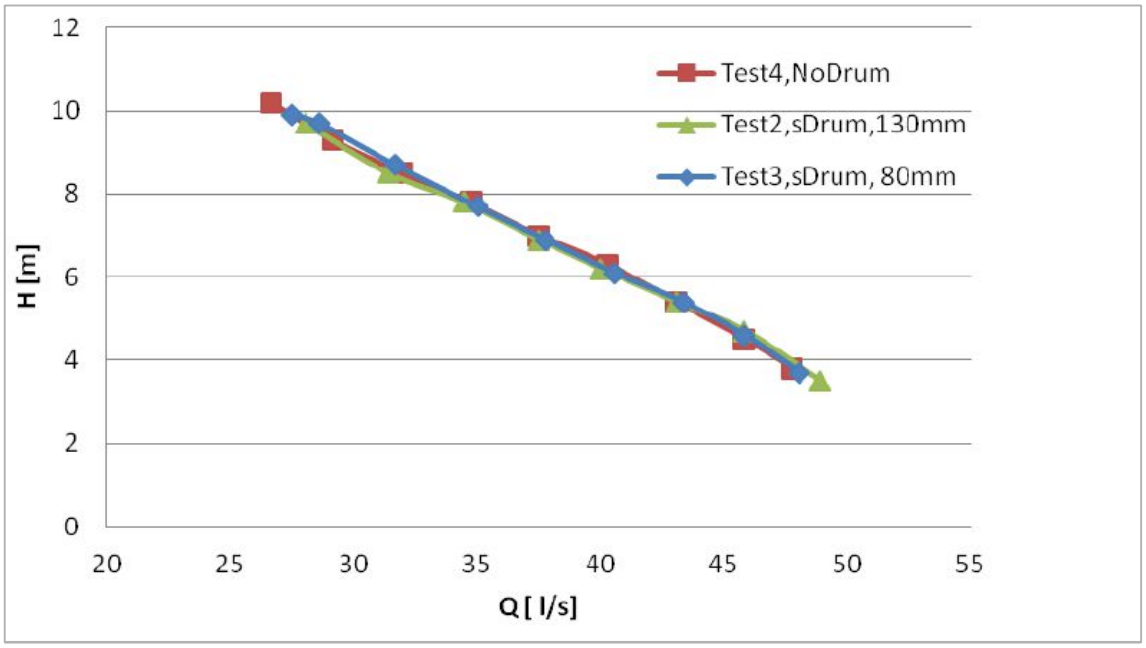

Figure 5-4 Pump Performance Comparison with Varied H/D Ratio (52)

This allows direct comparison between the computational results and experimental performance data for the pump as per the ISO9906 Gr2 Annex A2 test standard.

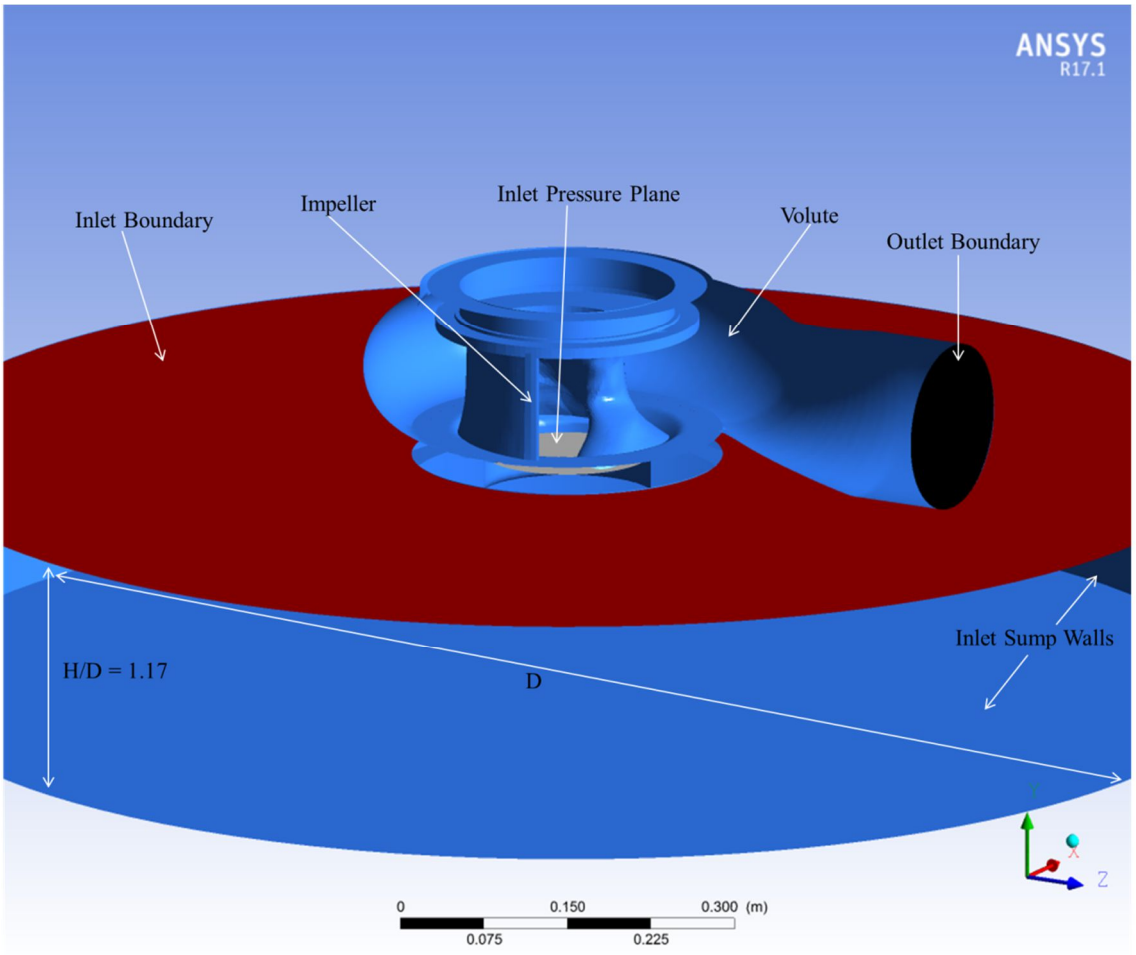

Figure 5-5 Simulated pump domain including inlet sump

5.6 Simulation

Table 5-1 Fluid and geometric properties

Fluid Properties [water at 20°C]	Density	$\rho = 998\ \mathrm{kg/m^3}$
	Dynamic viscosity	$\mu = 108 \times 10^{-5} kg/m \cdot s$
Universal Constant	Acceleration of gravity	$g = 9.81 m/s^2$
Pump layout	Elevation from inlet to outlet	$z_2 - z_1 = 1.381 m$
Boundary conditions	Impeller rotational speed	$\Omega = 150.8\ rad/s$
	Outlet Pressure	$p_2 = 0\ Pa$

A full pump simulation was carried out on the selected machine. The three flow rates at which the pump was tested in the experimental study were simulated. The maximum allowed timestep size is one that is sufficient to capture the movement of one cell in the rotor relative to the stator every timestep. As Lucius et al (53) state LES and DES models require higher levels of refinement than typical RANS models. The timestep used in this study was 1×10^{-5}, which is sufficient to capture transient behaviour, momentum transfer across the GGI and resolve wall bounded shear layer interaction at both rotor and stator. A timestep of this size also helps to make the solution more robust as the solver has more gradual changes to solve in between each timestep.

6 CFD Results and Discussion

6.1 Validation

The pump was simulated for a minimum of 6 impeller revolutions and the average pressure and velocity values over the last rotation were used to calculate pump head with Eq.8.

$$Hp = \frac{p_2 - p_1}{\rho g} + z_2 - z_1 + \frac{v_2^2 - v_1^2}{2g} \tag{8}$$

The results for computational head were then compared with head and flow from the experimental pump curve. The results of this can be seen in Figure 6.1, where head and flow have been normalised to best efficiency point where $Q^* = \frac{Q}{Q_{BEP}}$.

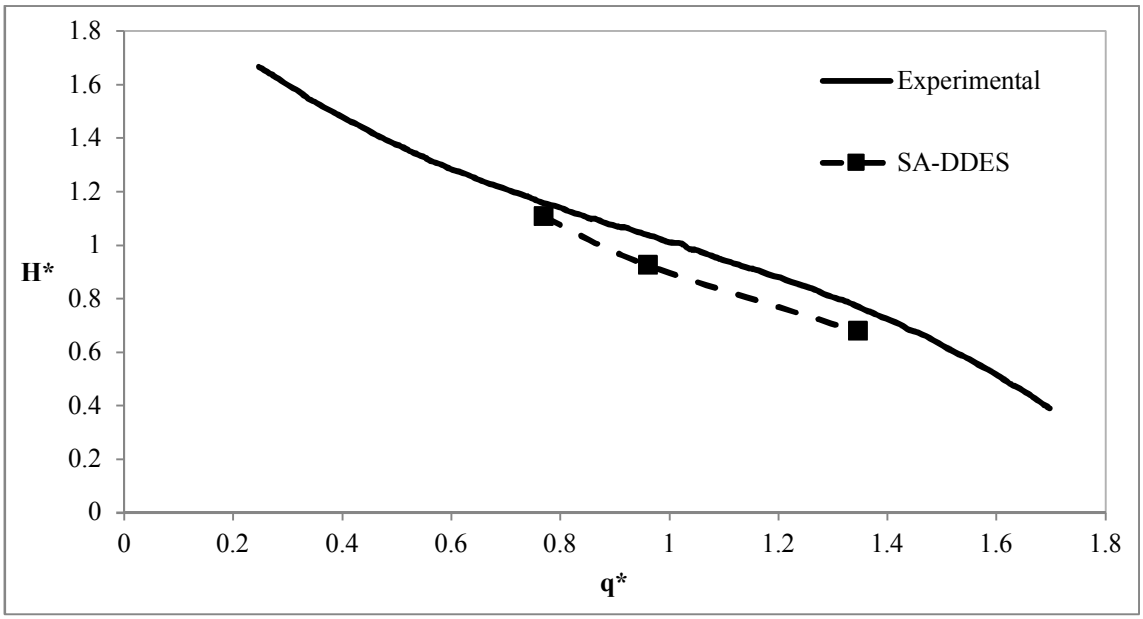

Figure 6-1 Computational Validation against Experimental Results

The validation of the computational curve versus the experimental curve shows that the predicted pump head from CFD at Q_{BEP}-30%, Q_{BEP}, and Q_{BEP}+30% is 4%, 11% and 13% respectively. Generally an acceptable level for quantitative analysis is ≤10%. Direct

comparison is not as important in this case as a qualitative analysis is being carried out rather than a quantitative study.

6.2 Velocity Components

Results were post processed in ANSYS CFD post. In addition to the inlet pressure plane mentioned in Chapter 5 a number of other analysis planes were inserted in the domain to study the fluid around the blade and volute at each flow rate [Figure 6.2] [Table 6.1].

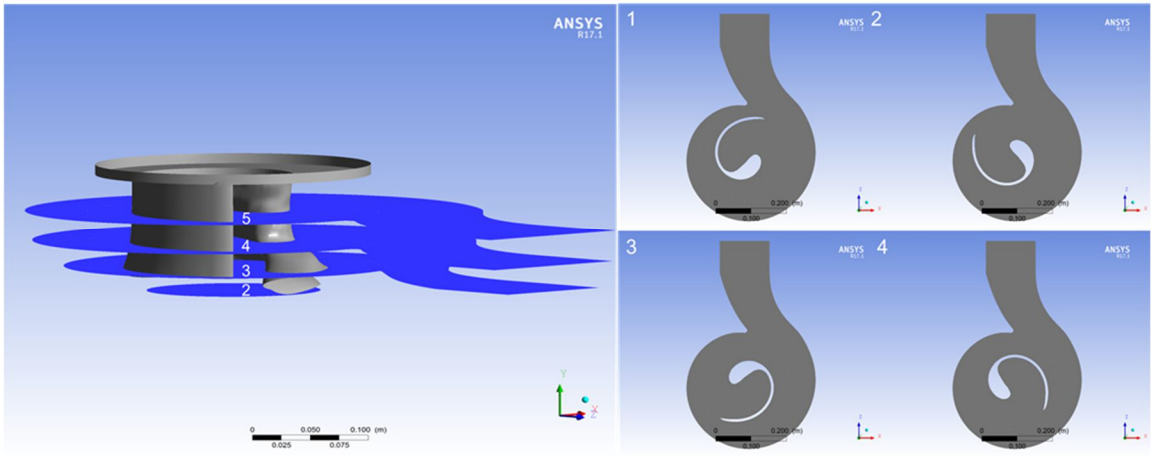

Figure 6-2 Left, Projection view of Impeller and 4 Analysis Planes. Right, Cross Section of Flow Domain at 4 Impeller Positions

Table 6-1 Plane locations on vertical position in the domain

Plane Number	Plane 2	Plane 3	Plane 4	Plane 5
Y position (m)	0.0328315	0.0567995	0.0567995	0.1126

Observations made during the experimental part of this work found that leading edge blockage was most prevalent at the coincident locations of the area where analysis planes 4 and 5 can be seen in Figure 6-2. Plane 2 was chosen in order to analyse the flow at the pump inlet, while plane 3 was chosen to examine why no blockage was seen at this area

of the pump. This could be theorised as being due to varying flow incident angles relative to the impeller leading edge as illustrated by [Fig 6-3] (54). This theory would also explain varying blockage performance at different flow rates, as noted in the experimental results in Chapter 4, and explained in section 6.3. (55)

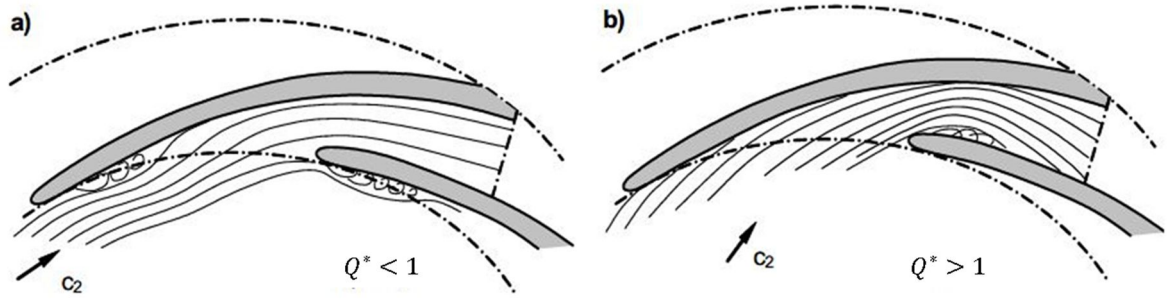

Figure 6-3 Differing β_1 at Impeller Leading Edge for Different Flow Rates, (54)

Based on the above theory, the fluid velocity was decomposed into radial and tangential components. Doing this allowed inspection of the velocity at each of the analysis planes in terms of moving circumferentially (tangentially in an instantaneous frame), v_{tan} [Eq. 9], with the impeller leading edge with potential for blockage or radially, v_{rad} [Eq. 10] outwards, away from the impeller leading edge and clearing the pump.

$$v_{tan} = -\frac{r_z}{\sqrt{r_x^2 + r_z^2}} V_x + V_z \frac{r_x}{\sqrt{r_x^2 + r_z^2}} \tag{9}$$

[Eq. 9] is expressed in CFD post using the CEL format as;

"-(Z/sqrt(X^2+Z^2))*Velocity in Stn Frame u + (X/sqrt(X^2+Z^2))*Velocity in Stn Frame w"

$$v_{rad} = \frac{r_x}{\sqrt{r_x^2 + r_z^2}} V_x + V_z \frac{r_z}{\sqrt{r_x^2 + r_z^2}} \quad (10)$$

[Eq. 10] is expressed in CFD post using the CEL format as;

"X/(sqrt(X^2+Z^2))*Velocity in Stn Frame u+Z/(sqrt(X^2+Z^2))*Velocity in Stn Frame w"

6.3 Discussion of Computational Results

Analysing v_{rad} and v_{tan} on the analysis planes specified in section 6.2, some interesting comparisons can be seen between the results observed in the experimental research and the theories deduced from the results. There appears to be a relationship between the ratio of radial to tangential planar velocity and the probability of blockage occurring. This is based on comparing a flow rate where blockage is more likely to occur with a flow rate where the pump does not block. This comparison can be seen in Figure 6-4.

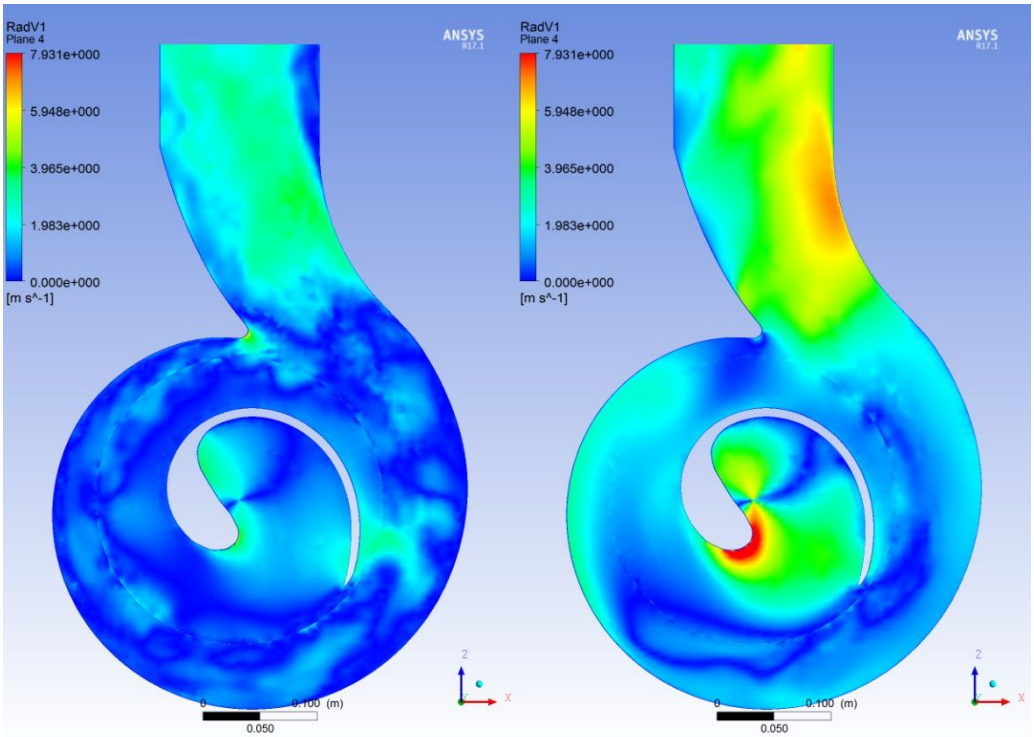

Figure 6-4 v_{rad} on Plane 4 at Q*=0.68(left) and Q*=1.11(right)

Figure 6-4 shows a much higher value of radial velocity at high flow rate compared to low flow rate. An area of high radial velocity can clearly be seen at the impeller leading edge where the relative flow incident angle at the impeller leading edge β_{1-en} is higher, as described by Paresh (56). This essentially means that as the flow rate changes the fluid incidence angle relative to the impeller leading edge also changes. Conversely, as Q* increases, tangential velocity decreases, [Figure 6-5]. This is in line with (55) and also the experimental results, validating the CFD approach. One hypothesis for an inverse relationship between Q* and v_{tan} is that there is less through-flow at low flow rates but very similar impeller rotational speed, causing a higher level of recirculation. As the fluid will remain for longer time in the domain at low flow, there is a longer time for the impeller to impart energy on to the fluid. Also as separation on the pressure surface is less likely to happen at low flow rates (57), the fluid may be more likely to stay attached to the blade allowing more transfer of angular momentum. The higher levels of recirculating flow can only serve to increase the probability of blockage due to the fact that the impeller is exposed to the rag for a longer time while rotating with the impeller. This is particularly true if the trailing part of a longer rag is still within the leading edge region of the impeller, slowing its ejection into the outer part of the volute. The impeller leading edge is then more likely to catch up with the rag.

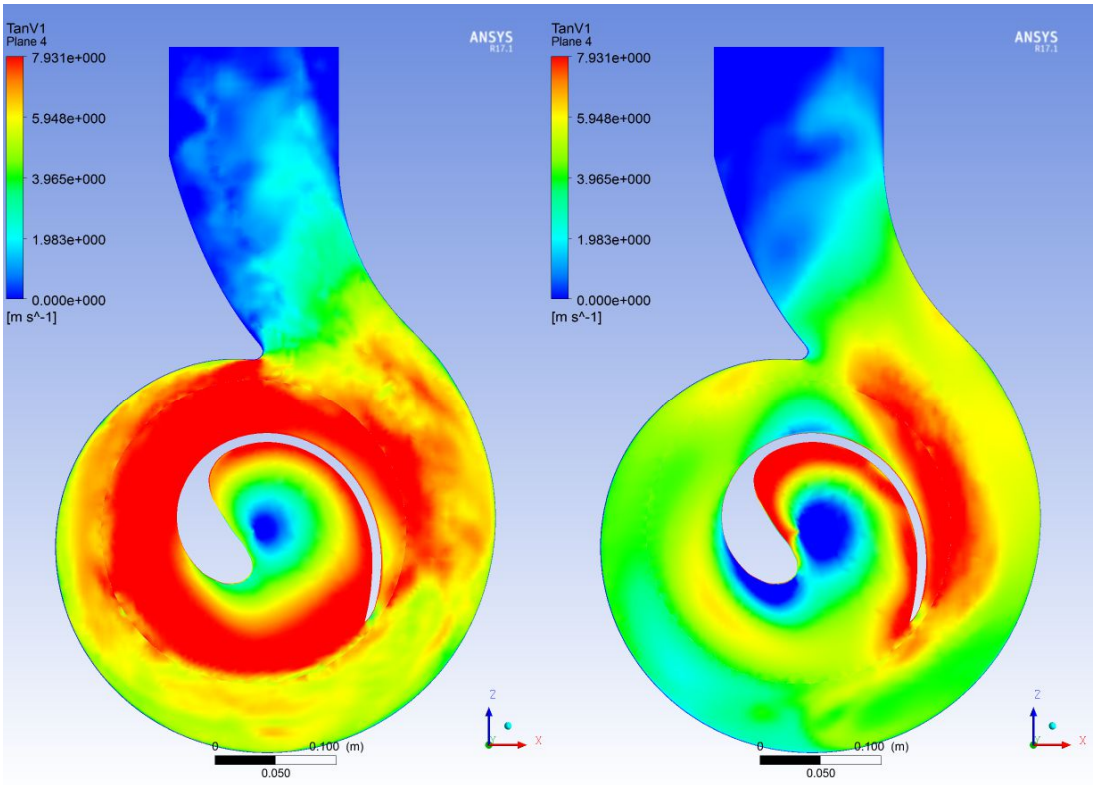

Figure 6-5 Tangential Velocity on Plane 4 at Q*=0.68(left) and Q*=1.11(right)

Figure 6-5 shows a much higher incidence of tangential velocity at low flow rate compared to high flow rate. This also corroborates the theory based on experimental results. Being that as the fluid is more inclined to recirculate the rag has a higher probability of impacting the leading edge and blocking the impeller. The low level of tangential velocity existing at the leading edge at Q*=1.11 where high radial velocity is present in Figure 6-3, makes it possible to infer that the flow is almost purely radial.

What is notable, especially in the high flow condition, is the occurrence of two areas of high tangential velocity [Figure 6.5]. The region of high v_{tan} on the suction surface of the impeller is caused by the flow following the curvature of the impeller and the flow incident angle.. The other area of high tangential velocity is caused by the impeller accelerating the fluid, due to centrifugal force, tangentially towards the volute outlet. Studying other positions of the impeller relative to the volute demonstrates similar occurrences [Figure 6-6].

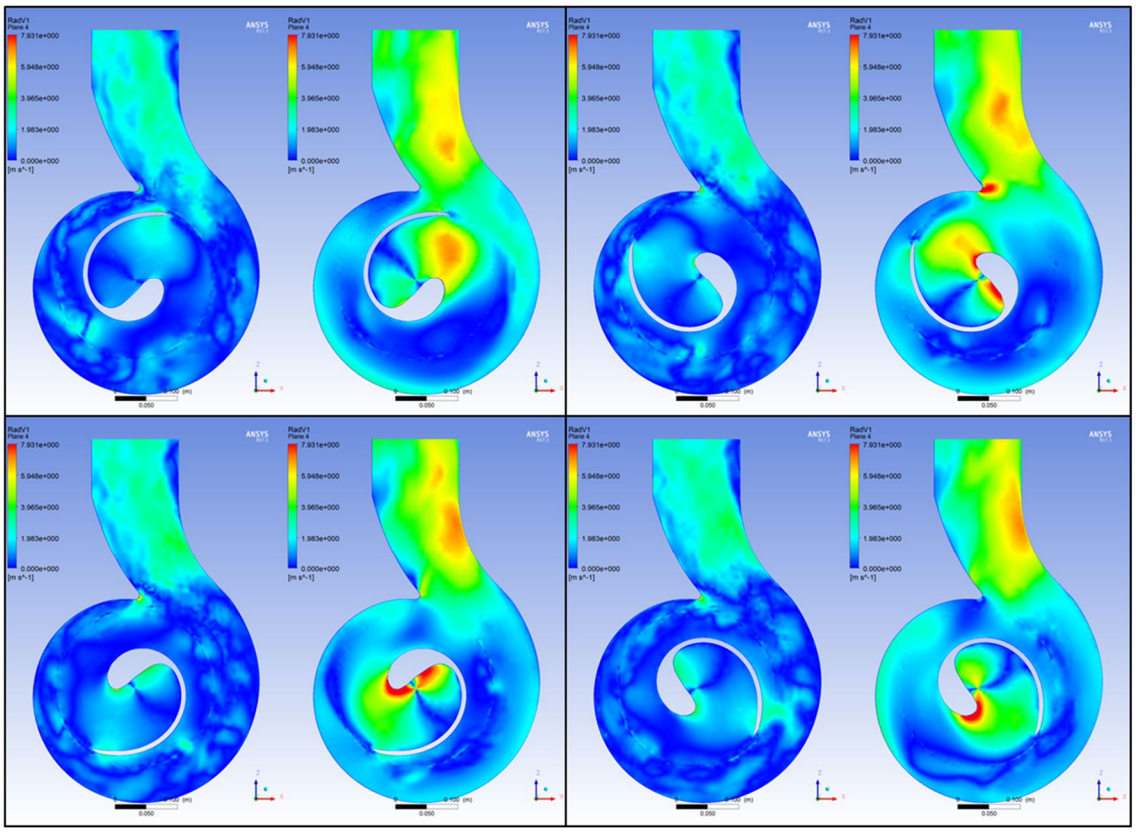

Figure 6-6 Radial Velocity at Q*=0.68(left) and Q*=1.11(right) for each of the four impeller positions studied.

Observing the radial velocity on both impellers shows the difference in radial velocity over the whole leading edge. This clearly illustrates the increase in radial velocity component proportionally to the flow rate [Figure 6-7]. This should contribute to the rag being more quickly ejected away from the leading edge at high flow rate compared to lower flow rate. When compared with experimental observations made with the high speed camera it is clear that rather than being caught either side of the leading edge and blocking, the rag when subjected to higher radial velocity components has now been moved clear of the leading edge.

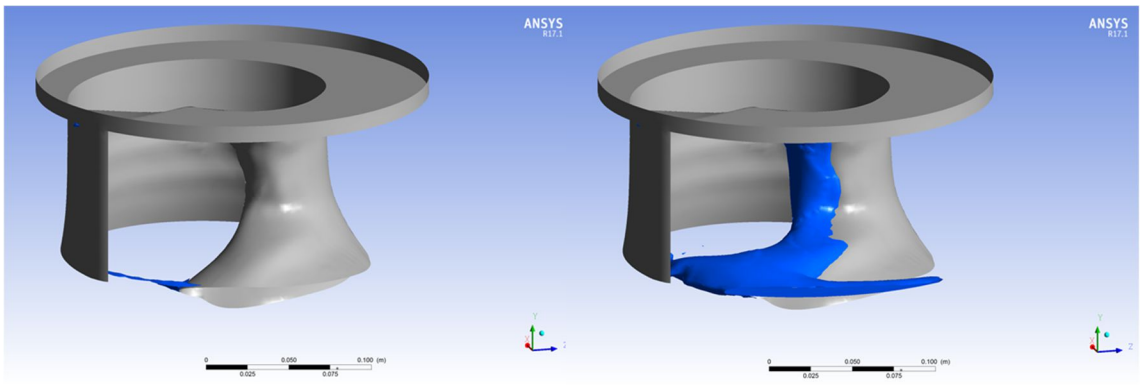

Figure 6-7 Isosurface of V_{rad} = 8m/s at Q*=0.68(left) and Q*=1.11(right) at position 3

Viewing all analysis planes gives more insight into how the region of high radial velocity looks throughout the domain [Figure 6-8] and explains the shapes of the isosurface in [Figure 6-7]. This shows highest distribution of high v_{rad} towards the large forward swept area of the blade, which was found to be unlikely to block in Section 4.2.

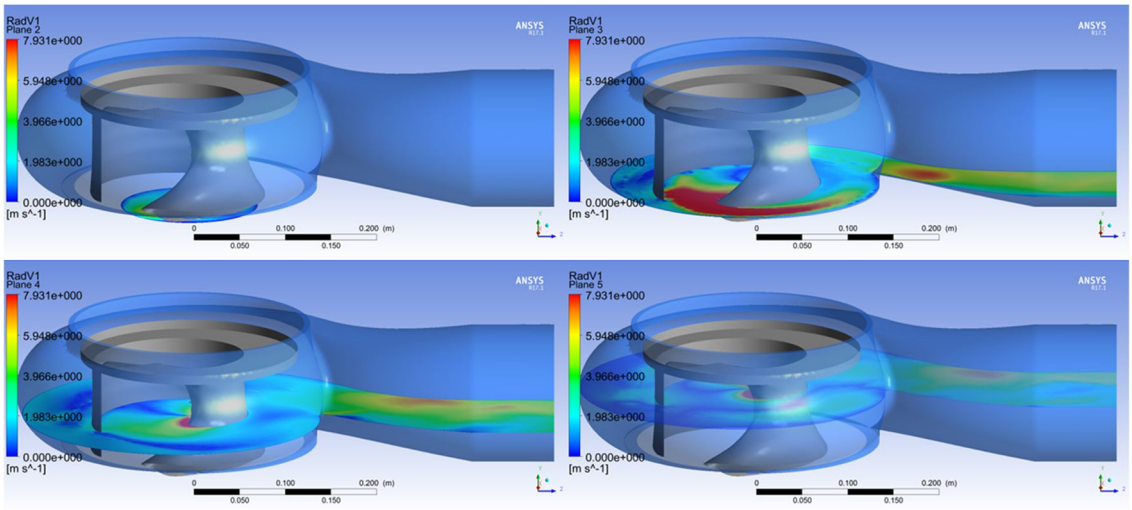

Figure 6-8 Each Analysis Plane at $Q_{bep+30\%}$ Highlights distrubution of v_{rad} in the Domain and the Basis for the Shape of Isosurface in Fig 6-7

It is important to also consider the inlet flow field, as this can be assumed to be an important factor in how the rag is presented to the pump impeller. Relatively higher radial velocity can also be observed at analysis plane 2, at the pump inlet at high flow rate, when

compared to low flow rate [Figure 6-9]. It could be put that regardless of rag position or orientation when entering the pump, a strong radial flow will help to move it outwards past the impeller leading edge once it has passed through the inlet.

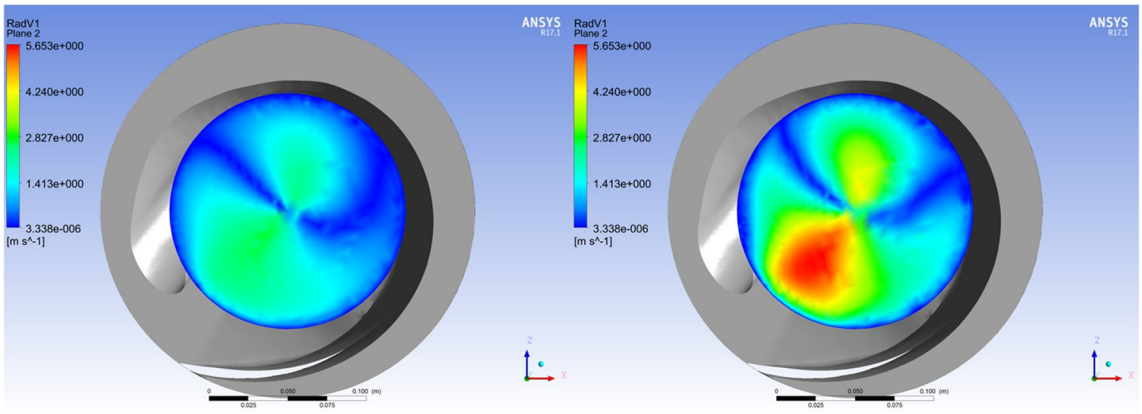

Figure 6-9 v_{rad} at pump inlet plane at Q*=0.68(left) and Q*=1.11(right)

Considering both contour plots and isosurfaces provides very good comparative evidence and helps to inform the overall behaviour of the flow. A comparison of velocity components in the domain provides a better quantitative description of how these components vary with flow rate, most importantly at the impeller leading edge, the area of the pump with the highest probability of blocking. To further investigate the relationship between v_{rad} and v_{tan} at high and low flow rates, a rake line was imposed onto analysis plane 4, 11mm in advance of the impeller leading edge, as shown in [Figure 6-10].

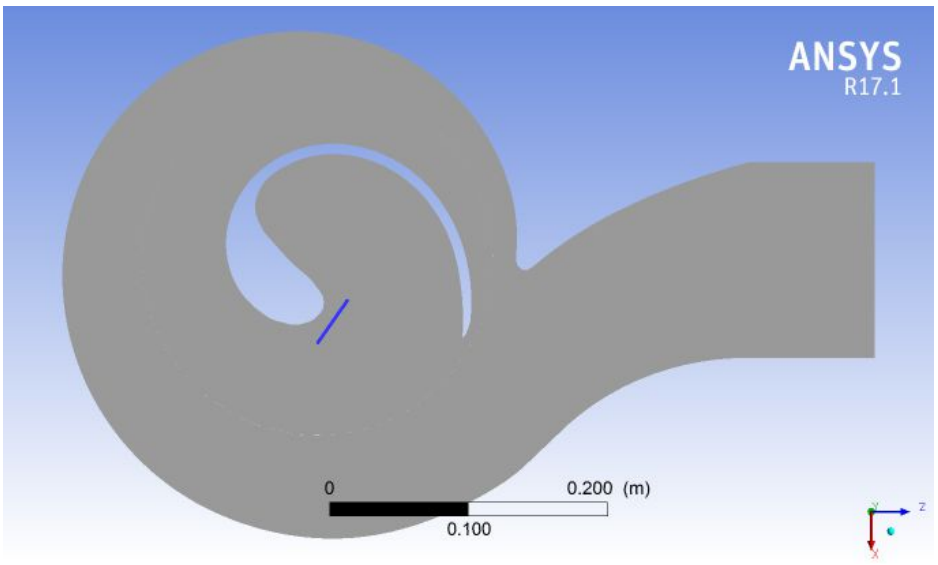

Figure 6-10 Rake line on plane 4 at impeller position 1

A rotation matrix was used to perform a rotational transformation on the rake line in order to consistently study comparable velocity profiles at each of the 4 impeller positions [Eq. 15].

$$\begin{bmatrix} x' \\ y' \end{bmatrix} = \begin{bmatrix} cos\theta & -sin\theta \\ sin\theta & cos\theta \end{bmatrix} \begin{bmatrix} x \\ y \end{bmatrix} \tag{11}$$

Plotting profiles of v_{rad} and v_{tan} at each impeller position shows the difference between each velocity type at both flow rates at impeller position 1, [Figure 6-11]. It is clear to see that v_{rad} is the most prevalent velocity component at high flow rate by as much as a factor of 2. Conversely, at low flow rate v_{tan} is the dominant component by 3-5 times. Also notable is when the same comparison is made at impeller position 4 [Figure 6-12] the difference between both components is higher at both flow rates. This indicates that blockage may be more likely to occur at impeller position 1 than at impeller position 4. The instantaneous rotational velocity of the leading edge, v_{rot}, at each position is important to consider relative to v_{rad} and especially v_{tan} as it highlights how quickly the impeller will catch up with the rag before it can be ejected into the volute.

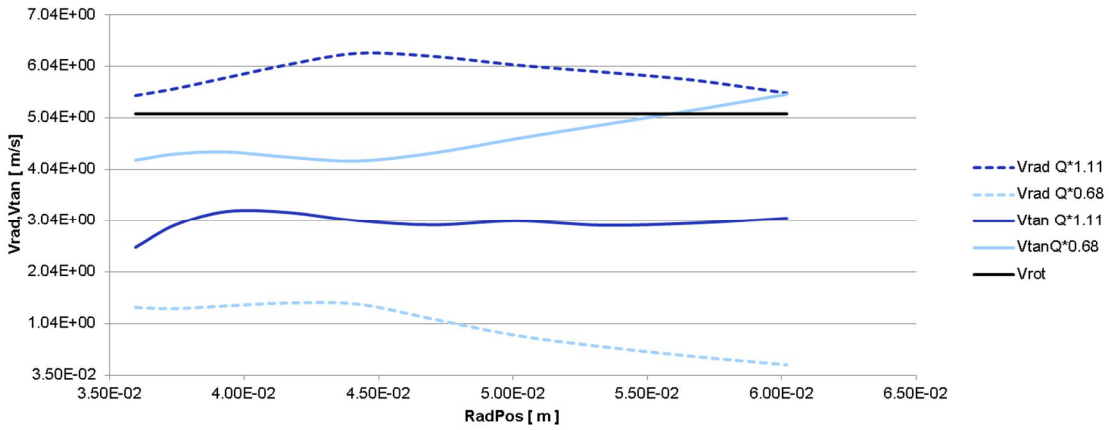

Figure 6-11 v_{rad}, v_{tan} on Impeller Rake Line and Leading Edge Rotational Speed, v_{rot} at Impeller Position 1

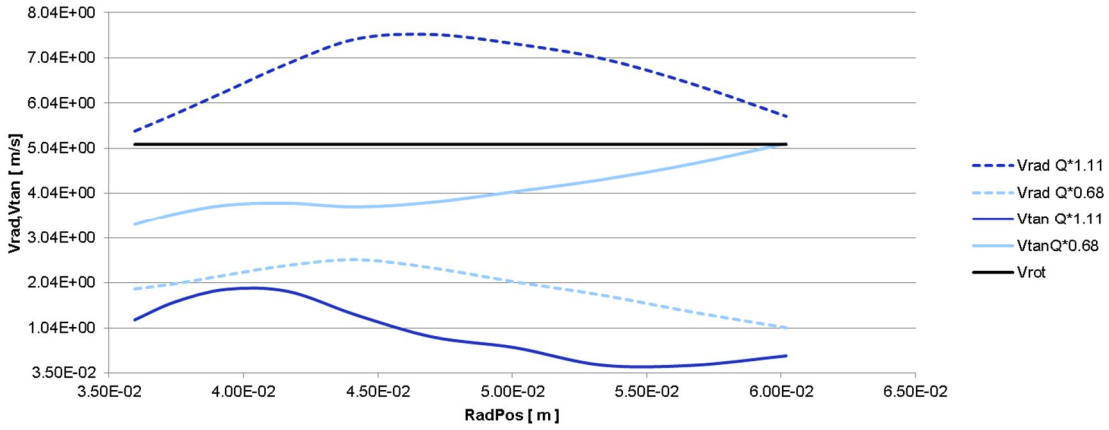

Figure 6-12 v_{rad}, v_{tan} on Impeller Rake Line and Leading Edge Rotational Speed, v_{rot} at Impeller Position 4

What is also notable is that v_{rad} is higher than the impeller rotational speed at all points on the leading edge rake line. It can be put forward that as v_{rad} is the dominant velocity at high flow rate even compared to the impeller rotational speed. The rag can move out of the way more quickly than the impeller can catch it [Figures 6-11, 6-12]. Furthermore if v_{tan} is greater than v_{rot} then the impeller should never catch up with the rag. As this has not been observed over the entire course of testing it can be concluded that v_{tan} is not a key variable for blockage performance and $v_{rad}$is.

7 Conclusions and Recommendations

7.1 Conclusions

In this study a comparison of experimental analysis has shown that most pumps perform better at resisting soft blockage at high flow rates compared to low flow rates. A new test rig was designed and a new test material was chosen in order to compare pumps of different sizes and at different design points. An analysis of factors which may contribute to blockage resulted in a dimensionless number which could in future be used to describe how probable a pump is to block while also informing future designs. As some factors identified are difficult to change due to the potential effects on performance, there are limitations on what designs are practically achievable.

Based on these results an observational analysis was performed with high speed photography at each flow rate with all test pumps to inform on the possible causes of soft blockages. Different types of blockage were identified and the main type of hydraulic blockage, leading edge blockage was highlighted for further study with CFD.

The CFD analysis at numerous flow rates showed a high contrast between flow angles within the pump and when the flow velocity was decomposed into its radial and tangential components a clear explanation for why soft blockage occurs became apparent. This is caused by the prevalence of radial velocity at higher flow rates which moves the rag outwards radially, away from the leading edge before contact can occur. A prevalence of high tangential component at low flow rates has shown that the rag has little radial force moving it outwards and a strong likelihood to recirculate, leading to blockage. It was also put forward that impeller position in the volute can have an effect on blockage performance. This may not be significant in physical testing, as the average inlet velocity at Q*=1.11 is $3.87 m/s$, compared with a leading edge velocity of $4.7 m/s$. By the time the rag has travel 40 mm through the inlet of the pump the impeller has already rotated by 90.4˚.

This work has shown the potential areas to concentrate on, concerning designing wastewater pump impellers. Designing pumps that are less likely to block will increase overall performance, reliability and lower cost for the operator.

7.2 Future Work

There is a scope for future work in this topic, most importantly;

- Detailed Geometry Study

  A parametric study of the impeller geometry could be investigated further. The area which seems to show most promise is the impeller leading edge as it is both most vulnerable to blockage and has the most impact on local fluid velocity in this area. A study surrounding variance in impeller β_1 with respect to blockage could yield interesting results.

- Rag/Inlet/Impeller Orientation

  In the experimental analysis to grade pump blockage performance, some variability was observed relating to the rag orientation at the pump inlet. A study on the effects of samples at different inlet locations on pump blockage would better inform on how sensitive the pump may or may not be to these factors. Further, better inlet/sump design could help to improve blockage performance.

- Impeller Position

  It was noted that impeller position in the volute affects the radial and tangential velocity components due to the transient nature of the operation of a single channel centrifugal pump. A study to observe the significance of impeller position on pump blockage could better inform future work.

- Rag Incidence

  Rag incidence was put forward as a means of analysing different parameters relating to the pump and rag and the potential for pump blockage. While some correlation was demonstrated, a dedicated study with a larger sample size could provide results with less noise.

8 Bibliography

1. **McEvoy, Richard.** *Innovative Development of Single-Blade-Impeller Hydraulics for Wastewater Application.* Limerick : University of Limerick, 2011.

2. **JMP.** WHO/UNICEF Joint Monitoring Programme for Water Supply and Sanitation. *WWSINFO.* [Online] October 2016. http://www.wssinfo.org/definitions-methods/.

3. **Korving, Hans et al.** Statistical Modelling of the Serviceability of Sewage Pumps. *Journal of Hydraulic Engineering.* 2006, Vol. 132, 10, pp. 1076-1085.

4. **Ashley, R et al.** Sustainable Disposal of Domestic Sanitary Waste. *Journal of Environmental Engineering.* Febuary 2005, Vol. 131, 2, pp. 206-215.

5. **Health Research Inc.** *Policies for the Design, Review, and Approval of Plans and Specifications for Wastewater Collction and Treatment Facilities.* Wastewater Committee of the Great Lakes, Upper Missippi River Board of State and Provincial Public Health and Environmental Managers . Albany, NY : Health Research Inc., 2004. Industry.

6. **Breen, Ben.** Pumps Engineered for Extremes. *Sulzer Technical Review.* 2014, 2.

7. **Caldwell, Chris.** *Pump Ed 101.* [Online] August 2012. http://www.pumped101.com/TB-G01-001%20Effex%20vs%20Experior%20part1.pdf.

8. **Karassik, Igor.** *Pump Handbook.* New York : McGraw-Hill, 2001.

9. **Chadwick, Andrew.** *Hydraulcis in Civil and Environmental Engineering.* London : SPON, 2008.

10. **Epple, Ph.** A Theorectical Derivation of the Cordier Diagram for Turbomachines. *Journal of Mechanical Engineering Science.* 2011, pp. 354-368.

11. **Stepanoff.** *Centrifugal and Axial Flow Pumps.* Florida : Krieger, 1957.

12. **Douglas, J.F.** *Fluid Mechanics.* Singapore : Longman, 1995.

13. **Shabayek, Shazy A.** Improving Approach Flow Hydraulics at Pump Intakes. *International Journal of Civil & Environmental Engineering.* December, Vol. 10, 6.

14. **Bousquet, Yannick.** Analysis of the Unsteady Flow Field in a Centrifugal Compressor from Peak Efficiency to Near Stall with Full-Annulus Simulations. *Journal of Fluid Engineering.* 2014, Vol. 2014.

15. **Akin, O.** Interaction of Zones of Flow Seperation in a Centrifugal Impeller-Station Vane System. *Experiments in Fluids.* 1994, Vol. 17, 6.

16. **Schlichting, H.** *Boundary Layer Theory.* Washington DC : NACA, 1949.

17. **Massey, Bernard.** *Mechanics of Fluids.* Oxon : Taylor & Francis, 2008.

18. **Flack, R.D.** Turbulence Measurements in a Centrifugal Pump with a Synchronously Orbiting Impeller. *Journal of Turbomachinery.* 1992, Vol. 114.

19. **Cheah, K. W.** Numerical Flow Simualtion in a Centrifugal Pump at Design and Off-Design Conditions. *International Journal of Rotating Machinery.* 2007, Vol. 2007.

20. **Hornsby, Craig.** CFD - Driving Pump Design Forward. *World Pumps.* August 2002, pp. 18-22.

21. **Watanabe, Takayuki.** Simulation of Steady and Unsteady Cavitation on a Marine Impeller using a RANS CFD Code. *Fifth International Symposium on Cavitation.* 2003.

22. **Crocker, D. S.** CFD Modellingof a Gas Turbine Combustor From Compressor Exit to Turbine Inlet. *Journal of Engineering for Gas Turbines and Power.* 1999, Vol. 121, 1.

23. **Williams, J.** A Calibration Study of CFD for Automotive Shapes and CD. *Journal of Passenger Cars.* 1994.

24. **Baik, Jong-Jin.** A CFD Model for Simulating Urban Flow and Dispersion. *Journal of American Meteorology.* 2003, 8805.

25. **Khalafvand, S.S.** CFD Simulation of flow through heart: a perspective review. *Computer Methods in Biomechanics and Biomedical Engineering.* 2011, Vol. 14, 1.

26. **Versteeg, H K.** *An Introduction to Computational Fluid Dynamics, The Finite Volume Method.* Harlow : Pearson, 2007.

27. **Katz, Aaron.** Mesh Quality Effects on the Accuracy of CFD Solutions on Unstructured Meshes. *Journal of Computational Physics.* 2011, Vol. 230, 20.

28. **Spalart, P.R.** Strategies for Turbulence Modelling and Simulations. *International Journal of Heat and Fluid Flow.* 2000, Vol. 21, 3, pp. 252-263.

29. **Ingram, D. M.** Developments in Cartesian cut cell methods. *Mathematics and Computers in Simulation.* 2003, Vol. 61, 3-6.

30. **ANSYS Inc.** *Fluent Theory Guide.* Canonsberg : ANSYS, 2013.

31. **Tu, Jiyuan.** *Computational Fluid Dynamics: A Practical Approach.* Oxford : Elsevier, 2008.

32. **Murthy, J.Y.** *Numerical Methods in Heat, Mass and Momentum Transfer.* West Lafayette : Perdue University, 2002.

33. **Bartels, C.** Comparison between Direct Numerical Simulation and k-e Prediction of the Flow in a Vessel Stirred by a Rushton Turbine. *Proceedings of 10th European Conference on Mixing.* 2000, pp. 239-246.

34. **Menter, F.R.** Zonal Two Equation k-w Turbulence Models for Aerodynamic Flows. *AIAA Journal.* 1993, Vol. 32, 8.

35. **Spallart, P.** A one-equation Turbulence Model for Aerodynamic Flows. *La Recherche Aérospatiale.* 1992, Vol. 1994, 1.

36. **Menter, F.R.** *Best Practise: Scale-Resolving Simulations in ANSYS CFD.* Ottefing : ANSYS, 2012.

37. **Constaintinescu, G.** *Wall Models and Hybrid RANS-LES methods.* Iowa : University of Iowa, 2012.

38. **Smagorinsky, J.S.** General Circulation Experiments with Primitive Equations. *Monthly Weather.* 1963, pp. 99-164.

39. **Lohasz, Mate Marton.** LES of the Transitional Flow in a Miniature Centrifugal Pump. *The 14th International Conference on Fluid Flow Technologies.* 2009.

40. **F.R. Menter, M kuntz, R. Langtry.** *Ten Years of Industrial Experience with the SST Turbulence Model.* Danbury : Begell House Inc., 2003.

41. **Elsevier.** www.scopus.com. *www.scopus.com.* [Online] Elsevier, October 2016. http://www.scopus.com.

42. **G. Pullan, J. Denton, M. Dunkley.** An Experimental and Computational Study of the Formation of a Streamwise Shed Vortex in a Turbine Stage. *International Gas Turbine and Aeroengine Congress and Exhibition.* 2003, Vol. 125, 2, pp. 291-297.

43. **Petit, Olivier.** The ERCOFTAC Centrifugal Pump OpenFOAM Case-Study. *3rd IAHR International Meeting of the Workgroup on Cavitation and Dynamic Problems in Hydraulic Machinery and Systems.* 2009.

44. **H. Jasak, M. Beaudoin.** OpenFOAM Turbo Tools: From General Purpose CFD to Turnomachinery Simualtions. *2011 Joint Fluids Engineering Conference.* 2011.

45. **Smits, Alexander J.** *Flow Visualization: Techniques and Examples.* London : Imperial College Press, 2012.

46. **Kevin A Kaupert, Thomas Staubli.** The Unsteady Pressure Field in a High Specific Speed Centrifugal Pump Impeller. *Journal of Fluids Engineering.* 1999, Vol. 121, 3, pp. 621-632.

47. **B. de Souza, A. Niven, R. McEvoy.** A numerical investigation of the Consant Velocity Volute Design Approach as Applied to the Single Blade Impeller. *Journal of Fluids Engineering.* 2010, Vol. 132, 6, p. vol. 132.

48. **Issa, R.** Solution of the Implicitly Discretised Fluid Flow Equations by Operator-Splitting. *Journal of Computational Physics.* 1986, Vol. 62, 1, pp. 40-65.

49. **Barton, I.E.** Comparison of SIMPLE and PISO Type Algorithms for Transient Flows. *International Journal for Numerical Methods in Fluids.* 1998, Vol. 26, 4, pp. 459-483.

50. **Delauré, Y.** *CFD Modelling of Turbulent Incompressible Flow for Pumping/Mixing Applications.* Dublin : s.n., 2016.

51. **Nichols, R.H.** *Turbulence Models and Their Application to Complex Flows.* Birmingham : University of Alabama, Rev 4.01.

52. **Albadawi, Abdulaleem.** *Pump Performance Tests with Inlet Systems.* Dublin : Dublin City University, 2015.

53. **A. Lucius, G Brenner.** Numerical Simulation and Evaluation of Velocity Fluctuations During Rotating Stall of a Centrifugal Pump. *Journal of Fluids Engineering.* 2011, Vol. 133, 8.

54. **Gülich, Johann Friederich.** *Centrifugal Pumps.* Heidelberg : 2008, 2008.

55. **J. Feng, F.-K Benra, H.J Dohmen.** Unsteady Flow Visualisation at Part-Load Conditions of a Radial Diffuser Pump: by PIV and CFD. *Journal of Visualization.* 2009, Vol. 12, 1, pp. 65-72.

56. **Paresh Girdhar, Octo Moniz.** *Practical Centrifugal Pumps.* Oxford : Elsevier, 2011.

57. **Rikke K. Byskov, Christian B. Jacobsen, Nicholas Pedersen.** Flow in a Centrifugal pump Impeller at Design and Off-Design Conditions - PartII: Large Eddy Simulations. *Journal of Fluids Engineering.* 2003, Vol. 125, 1.

58. **G. Bluman, S.Kumei.** *Symmetries and Differential Equations.* New York : Springer, 1989.

59. **Menter, F.R.** Adaption of Eddy Viscosity Turbulence Models to unsteady Separated Flow Behind Vehicles. *Lecture Notes in Applied and Computational Mechanics.* 2003, Vol. 19.